Evolution of OH reactivity in low-NO volatile organic compound photooxidation investigated by the fully explicit GECKO-A model

Zhe Peng[1], Julia Lee-Taylor[1,2], Harald Stark[1,3], John J. Orlando[2], Bernard Aumont[4] and Jose L. Jimenez[1]

[1] Department of Chemistry and Cooperative Institute for Research in Environmental Sciences, University of Colorado, Boulder, Colorado 80309, USA

[2] Atmospheric Chemistry Observation and Modeling Laboratory, National Center for Atmospheric Research, Boulder, Colorado 80307, USA

[3] Aerodyne Research Inc., Billerica, Massachusetts 01821, USA

[4] Univ Paris Est Créteil and Université de Paris, CNRS, LISA, F-94010 Créteil, France

Correspondence: Zhe Peng (zhe.peng@colorado.edu) and Jose L. Jimenez (jose.jimenez@colorado.edu)

Abstract. OH reactivity (OHR) is an important control on the oxidative capacity in the atmosphere but remains poorly constrained in many environments, such as remote, rural, and urban atmospheres, as well as laboratory experiment setups under low-NO conditions. For an improved understanding of OHR, its evolution during oxidation of volatile organic compounds (VOCs) is a major aspect requiring better quantification. We use the fully explicit Generator of Explicit Chemistry and Kinetics of Organics in the Atmosphere (GECKO-A) model to study the OHR evolution in the low-NO photooxidation of several VOCs, including decane (an alkane), m-xylene (an aromatic), and isoprene (an alkene). Oxidation progressively produces more saturated and functionalized species. Total organic OHR (including precursor and products, OHR_{VOC}) first increases for decane (as functionalization increases OH rate coefficients), and m-xylene (as much more reactive oxygenated alkenes are formed). For isoprene, C=C bond consumption leads to a rapid drop in OHR_{VOC} before significant production of the first main saturated multifunctional product, i.e., isoprene epoxydiol. The saturated multifunctional species in the oxidation of different precursors have similar average OHR_{VOC} per C atom. The latter oxidation follows a similar course for different precursors, involving fragmentation of multifunctional species to eventual oxidation of C1 and C2 fragments to CO_2, leading to a similar evolution of OHR_{VOC} per C atom. An upper limit of the total OH consumption during complete oxidation to CO_2 is roughly 3 per C atom. We also explore the trends in radical recycling ratios. We show that differences in the evolution of OHR_{VOC} between the atmosphere and an environmental chamber, and between the atmosphere and an oxidation flow reactor (OFR) can be substantial, with the former being even larger, but these differences are often smaller than between precursors. The Teflon wall losses of oxygenated VOCs in chambers result in large deviations of OHR_{VOC} from atmospheric conditions, especially for the oxidation of larger precursors, where multifunctional species may suffer substantial wall losses, resulting in significant underestimation of OHR_{VOC}. For OFR, the deviations of OHR_{VOC} evolution from the atmospheric case are mainly due to significant OHR contribution from RO_2 and lack of efficient organic photolysis. The former can be avoided by lowering the UV lamp setting in OFR, while the latter is shown to be very difficult to avoid. However, the former may significantly offset the slowdown in fragmentation of multifunctional species due to lack of efficient organic photolysis.

1 Introduction

Photooxidation is a key process altering the concentrations of trace gases in the atmosphere (Levy II, 1971; Atkinson and Arey, 2003). It is also the main contributor to the formation of O_3 and secondary aerosols (Haagen-Smit, 1952; Chameides et al., 1988; Hallquist et al., 2009). Both products are major tropospheric pollutants (Nel, 2005; Cohen et al., 2017) and the latter have large climate impacts (Stocker et al., 2014).

Hydroxyl radical (OH) is the primary oxidizing agent in atmospheric photooxidation (Levy II, 1971). Its atmospheric fate is governed by the species that it reacts with, i.e., OH reactants. The first-order rate constant of OH consumption by an OH reactant is often called its OH reactivity (OHR), equal to the product of the reactant concentration and second-order rate constant with OH. Total OHR (OHR$_{tot}$), i.e., the sum of OHR across all OH reactants (OHR$_{tot}$ = $\sum_i (k_i * c_i)$), where k_i and c_i are the second-order rate constant with OH and concentration of the ith OH reactant), is the real first-order loss rate constant of OH.

OHR has been measured for over 20 years (Kovacs and Brune, 2001) in various settings, e.g., urban areas (Lu et al., 2013; Whalley et al., 2016), forested areas (Nölscher et al., 2016; Zannoni et al., 2016), and environmental chambers (Fuchs et al., 2013; Nölscher et al., 2014; Fuchs et al., 2017; Novelli et al., 2018). Despite numerous measurements and remarkable technical developments (Yang et al., 2016; Fuchs et al., 2017), a sizable fraction of total OHR in most measurements has not been chemically speciated, leading to so-called "missing reactivity" (Williams and Brune, 2015; Yang et al., 2016). Multiple studies (Nölscher et al., 2016; Whalley et al., 2016; Sato et al., 2017) have attributed missing reactivity to the highly complex mixture of intermediates and products of volatile organic compound (VOC) oxidation, most of which are oxygenated VOCs (OVOCs). Primary VOCs themselves have been found to be the largest contributor of the speciated OHR in many studies (Yang et al., 2016). In order to well understand ambient OHR, the evolution of OHR (including that from OVOCs) during primary VOC photooxidation thus needs to be investigated.

Experimentally, this can be done in environmental chambers. However, only a few such experiments have been published (Nakashima et al., 2012; Nehr et al., 2014; Nölscher et al., 2014; Sato et al., 2017), all under high-NO conditions, where the key organic radical intermediate in VOC oxidation, i.e., organic peroxy radical (RO$_2$), mainly reacts with NO. To our knowledge, no experiment of this type at low NO, where RO2 can substantially react with hydroperoxy radical (HO2), has been published so far, potentially partially due to the difficulty in experimentally ensuring that low-NO conditions are achieved in chambers (Nguyen et al., 2014). Also, many OVOCs, which may account for missing reactivity, have sufficiently low volatility to significantly partition to chamber walls (Matsunaga and Ziemann, 2010; Krechmer et al., 2016), further complicating these experiments. The OVOC wall losses also often limit operation times of chamber experiments to a few hours, after which the wall losses are so large that meaningful interpretation of experimental results would be difficult. Therefore, the highest equivalent photochemical age that can be reached in chamber experiments is also typically hours and far shorter than would be needed to explore the OHR evolution in later stages of VOC

79   oxidation.

80   Oxidation flow reactors (OFR) are an alternative to chambers with much smaller volume, shorter

81   residence time (and thus smaller wall losses of trace gases), and stronger oxidative capacity (Kang et

82   al., 2007; Brune, 2019; Peng and Jimenez, 2020). The most common version of OFR is equipped with

83   low-pressure Hg lamps emitting UV at 185 and 254 nm, which photolyzes water vapor, O_2, and O_3, and

84   generates a large amount of OH both directly and through subsequent radical reactions. High OH

85   concentration in OFR often leads to equivalent photochemical age of days to weeks (Li et al., 2015;

86   Peng et al., 2015). In principle, OFR can also be employed to explore OHR evolution in VOC oxidation.

87   However, OHR from VOC (OHR_{VOC}, from both precursor and oxidation intermediates/products, in which

88   we include CO as an "organic" product of VOC oxidation) can have strong impacts on oxidative capacity

89   (particularly OH concentration) and hence radical chemistry in OFR at both low (Li et al., 2015; Peng et

90   al., 2015) and high NO (Peng and Jimenez, 2017; Peng et al., 2018). Peng and Jimenez (2020) have called

91   for highly chemically detailed modeling of gas-phase organic chemistry in OFR to assess the impacts of

92   organic OH reactants on OH in a more quantitative manner.

93   In this study, we explore for the first time the OHR evolution in entire low-NO VOC photooxidation

94   processes by modeling. Since chemical mechanism incompleteness causes other models to

95   unsatisfactorily simulate measured OHR_{tot} (Williams and Brune, 2015), we use the fully chemically

96   explicit model GECKO-A (Generator of Explicit Chemistry and Kinetics of Organics in the Atmosphere)

97   (Aumont et al., 2005). We simulate the photooxidation of different types of VOCs in the atmosphere,

98   in chamber, and in OFR, to find out general trends of OHR evolution in VOC oxidation and whether VOC

99   oxidation chemistries in chamber and OFR are representative of that in the atmosphere in terms of

100   OHR evolution.

101   **2   Methods**

102   Here we first discuss the VOC precursor types and conditions selected for the model cases in this

103   study. Then we describe the GECKO-A model and present our additional mechanism, model, and

104   software development required for this study.

105   **2.1   Model cases**

106   The photooxidation of an alkane (decane), an alkene (isoprene), and an aromatic (m-xylene) is

107   investigated under a variety of conditions without any NO. In pristine regions such as open oceans, NO

108   has typical concentrations on the order of 1 ppt (Wofsy et al., 2021) and hence contribute only a few

109   percent to RO_2 loss (Peng et al., 2019). For simplicity, we choose not to maintain such a low NO level in

110   the simulations, but to model zero-NO cases instead. The model cases are listed in Table 1: i) two cases

111   under ambient conditions, one with constant sunlight at solar zenith angle of 45° and the other with

112   diurnally-varying solar radiation and a noontime solar zenith angle of 0°; ii) six cases under typical

113   chamber conditions, i.e., low (10 s-1) / high (100 s-1) precursor OHR without gas-particle-wall

114   partitioning, with gas-particle partitioning (no wall), and with gas-particle-wall partitioning; and iii) five

115   cases under OFR conditions, of which two conditions resulting in significant non-tropospheric organic

116   photolysis (Peng et al., 2016) and one leading to remarkable deviations of RO2 fate from that in the

117 troposphere are not recommended in practice, but are still included for completeness since they are
118 similar to conditions in some literature studies (Table 1).For the UV source in chamber cases, we adopt
119 the spectrum of the blacklight and fluorescence light array in the University of Colorado Environmental
120 Chamber Facility (CU Chamber; Krechmer et al., 2017). The CU Chamber has a volume of ~20 m3, a
121 surface area of ~65 m2, and an estimated wall condensation timescales of ~1000 s (Krechmer et al.,
122 2016). The parameterization for the reversible gas-wall partitioning is taken from Krechmer et al. (2016)
123 with updates of Liu et al. (2019). Wall partitioning in chambers at equilibrium is a function of the
124 surface-to-volume ratio (Krechmer et al., 2016). The timescale to approach equilibrium is expected to
125 be larger in larger chambers, but still far shorter than the long experiments needed to investigate high
126 photochemical ages. Therefore differences in wall partitioning timescale are not important for this
127 study. Figure S9 of Krechmer et al. (2016) compared the CU Chamber and a few other well-known
128 chambers (including very large ones such as EUPHORE (Siese et al., 2001) and SAPHIR (Rohrer et al.,
129 2005)), showing relatively small differences (within a factor of ~2 in terms of surface-to-volume ratio).
130 Therefore the conclusions about wall partitioning in this study should be approximately applicable to
131 most chambers. The cases under ambient conditions, and chamber conditions with low / high precursor
132 OHR are simulated for 10, and 6 / 30 d, respectively, to encompass an equivalent photochemical age
133 of >10 d in each case (given a typical average ambient OH concentration of $1.5x10^6$ molecules cm^{-3} in
134 the real atmosphere (Mao et al., 2009); see Fig. 1 for the correspondence between equivalent
135 photochemical age and OH exposure (OH_{exp}, i.e., the integral of OH concentration over time)). The
136 simulated OFR in the present work employs the light source parametrization obtained by Li et al. (2015)
137 and Peng et al. (2015). UV at both 185 and 254 nm is used to generate OH, i.e., the "OFR185" mode of
138 operation. The residence time in the OFR is always 3 min. Wall losses in the OFR should be smaller than
139 in the chamber, due to reduced wall contact (Brune 2019), and are not simulated here. As several key
140 parameters of the chamber and OFR cases were obtained experimentally at room temperature and
141 atmospheric pressure in Boulder, Colorado, USA (typically 295 K and 835 mbar), for an easier
142 comparison, we use these values for the temperature and atmospheric pressure of all model cases.

143 In addition, we simulate illustrative cases of methane oxidation, under ambient and OFR
144 conditions (Table 1 and Section 3.1). Note that these two simulations are performed using the GECKO-
145 A generated mechanism (see Section 2.2) in KinSim (Peng and Jimenez, 2019), a chemical-kinetics solver
146 that is not GECKO-A's default, to avoid possible numerical issues in the GECKO-A internal solver, as
147 methane oxidation by OH is very slow (Atkinson and Arey, 2003) and very long runs are needed.To
148 characterize trends of OHR evolution (see Section 3.5), the ambient cases with constant sunlight are
149 simulated for two more alkanes, i.e., butane and heptane (Table 1). To explore the effects of UV sources
150 in OFR (see Section 3.4), two simulations under a typical OFR condition with an additional broad-
151 spectrum UV source (5 and 10000 times the chamber UV source in this study, respectively) are
152 performed for isoprene (Table 1).

153 **2.2 The GECKO-A model**

154 GECKO-A (Aumont et al., 2005; with updates as described by Camredon et al., 2007; Valorso et

155 al., 2011; Lee-Taylor et al., 2015), is an explicit chemical model which uses known mechanisms and rates

156 supplemented with experimentally-based structure-activity relationships to generate comprehensive

157 atmospheric oxidation mechanisms for organic species. The mechanisms are implemented within a box

158 model with a two-step solver (Verwer, 1994; Verwer et al., 1996). In mechanism generation, isomer

159 lumping for mechanism reduction purposes is applied to certain products with branching ratios < 1%

160 (here typically N-containing products, which are not relevant for our simulations). It has a negligible

161 impact on the results.

162   The core isoprene scheme in GECKO-A is adopted from the Master Chemical Mechanism v3.3.1

163 (Jenkin et al., 2015), while the meta-xylene oxidation mechanism follows MCM v3.2 (Jenkin et al, 2003,

164 Bloss et al, 2005), typically until ring-breaking occurs, whereupon the GECKO-A mechanism generator

165 implements the standard SAR protocols as described by Aumont et al. (2005), Camredon et al. (2007),

166 and Lee-Taylor et al. (2015). Under the zero-NO conditions employed in this study, we find that, in two

167 of the four m-xylene reaction channels (xylenol, 17%; and MXYLO2, 4%), some product species persist

168 anomalously owing to lack of alternative reaction pathways in the MCM. We therefore allow GECKO-A

169 to apply the standard SARs to two cyclic non-aromatic products of xylenol (MXYOLO2 and MXYOLOOH

170 in the 51% xylenol OH-oxidation channel, see Scheme S1). We also introduce OH-oxidation of

171 MXYCATECH and MXY1OOH (in the 42% and 7% xylenol OH-oxidation channels), and of MXYLOOH and

172 MXYLAL (in the MXYLO2 channel), assuming similarity to the MCM OH-oxidation of xylenol to

173 MXYOLO2, and with net OH rate constants estimated using the EPA EPISuite software package (US EPA,

174 2012). MXYLOOH, MXCATECH and MXYLAL each yield between two and six bicyclic non-aromatic

175 substituted peroxy radicals, with net OH rate constants of 1.77×10^{-11}, 1.56×10^{-10} and 8.6×10^{-13} cm^3

176 $molecule^{-1}$ s^{-1} respectively. (The MXYLOOH OH-rate also includes MXYLAL production). MXY1OOH is

177 assigned a substituted single-ring hydroxy-ketone product, with OH rate constant 3.26×10^{-11} cm^3

178 $molecule^{-1}$ s^{-1}. The early part of the meta-xylene reaction scheme used in this work is shown in Scheme

179 S1.

180   We tested the effect of solver integration timestep length on output precision. The output

181 species concentrations in all simulations but for isoprene OFR (Table 1) converge well as integration

182 timestep decreases (Fig. S1). In the isoprene OFR test cases, the output values oscillate over a small

183 range (<~5%) for integration timesteps ≤ 0.01 s (Fig. S1). Since this numerical error is smaller than typical

184 rate constant measurement uncertainties (from ~10% to a factor of 2–3; Burkholder et al., 2015), let

185 alone the uncertainties related to the SARs used in GECKO-A, it is deemed acceptable for the relevant

186 simulations in this study. The integration timestep for each simulation in the present work is reported

187 in Table 1.

188   We allow mechanism generation to proceed through to CO_2 production in most cases in this

189 study. The only exception is for extremely low-volatility species (saturation vapor pressure < 10^{-13} atm)

190 which are considered to be completely and irreversibly partitioned to the particle phase. Particle- and

191 wall-phase species are no longer considered in the OHR budget, since heterogeneous oxidation is much

192 slower than gas-phase oxidation (e.g., George and Abbatt, 2010). Gas-particle-wall partitioning is

193   activated only for the chamber cases where wall effects are considered. For the ambient cases and the

194   chamber cases without gas-wall partitioning, gas-particle partitioning is also disabled to avoid artificial

195   condensation of gases into the particle phase. In environments with very low NO (e.g., remote

196   atmosphere), organic aerosol concentration is typically 0.2 µg m^{-3} (Hodzic et al., 2020) while most major

197   intermediates/products have higher saturation concentrations (C*) and hence largely stay in the gas

198   phase. C* is calculated using the parameterization of Nannoolal et al. (2008) (default option of GECKO-

199   A). Although SIMPOL (Pankow and Asher, 2008) was recommended by Krechmer et al. (2016) to

200   estimate C* for the chamber wall partitioning treatment using their parameterization, the C* estimates

201   by the Nannoolal and SIMPOL parameterizations are close (generally within a factor of 2) for the species

202   that can reversibly partition between the gas and wall phases (C* ~ 0.1–1000 µg m^{-3}) in this study. This

203   difference is smaller than the uncertainties of the Krechmer et al. (2016) parameterization. Therefore,

204   the use of the parameterization of Nannoolal et al. (2008) for C* estimation is acceptable.

205   Concerns have previously been expressed about non-conservation of carbon in GECKO-A

206   (Mouchel-Vallon et al., 2020). This has proven in the current simulations to be almost entirely due to

207   lack of accounting for product CO_2 in some handwritten reactions. We edited the handwritten isoprene

208   and m-xylene schemes (see above and Section 2.2.3) for carbon balance, which reduced simulation-

209   end carbon losses in the m-xylene and isoprene ambient cases with constant UV from 4% and 9%,

210   respectively, to negligible levels (<0.4%; Fig. S2).

211   For the current study, we have made several updates to GECKO-A, i.e., i) inclusion of key OFR-

212   specific radical reactions, ii) extension of the UV range considered to cover 185 and 254 nm, and iii)

213   updates to the low-NO m-xylene oxidation mechanism, so that GECKO-A is able to simulate OFR

214   chemistry and the entire process of low-NO m-xylene photooxidation (until CO/CO_2). We will describe

215   these three updates below.

216   **2.2.1 Key radical reactions in oxidation flow reactor**

217   We have added several reactions that are unimportant in the troposphere, but that are required

218   to fully represent the radical chemistry within the OFR (Li et al., 2015). The most important inorganic

219   reactions are H_2O + hv (185 nm) $\rightarrow$ H + OH, O_2 + hv (185 nm) $\rightarrow$ 2O(^{3}P), and O_3 + hv (254 nm) $\rightarrow$ O(^{1}D)

220   + O_2. These three reactions, together with O(^{3}P) + O_2 + M $\rightarrow$ O_3 + M and O(^{1}D) + H_2O $\rightarrow$ 2OH, which are

221   already in the GECKO-A inorganic radical chemistry scheme, are responsible for the OH generation in

222   OFR. The OFR radical chemistry has previously been modeled in detail using KinSim (Peng and Jimenez,

223   2019), which was validated against experimental observations (Li et al., 2015; Peng et al., 2015). A

224   comparison between KinSim and GECKO-A for a range of OFR conditions shows typical agreement

225   between the two models within 2% for key outputs.

226   Due to high OH in OFR, reaction of RO_2 with OH is also included in mechanism generation, with

227   an assumed rate constant of 1x10^{10} cm^3 molecule^{-1} s^{-1} (Peng et al., 2019). The products of this type of

228   reaction are assumed to be RO (alkoxy radical) + HO_2 for alkyl RO_2 and R (alkyl radical) + CO_2 + HO_2 for

229   acyl RO_2. Although these reactions for certain RO_2 may have reaction intermediates, the reactions of

230   the intermediates (with OH) are believed to be very fast under OFR conditions where OH is much higher

than in the atmosphere (Peng and Jimenez, 2020) and hence only the probable final products (no intermediates) of these reactions are included in mechanism generation. The reaction of RO_2 with OH is not included in the mechanisms for the ambient and chamber simulations due to low contribution of this pathway to the RO_2 fate in those cases.

2.2.2 Organic photolysis at 185 and 254 nm

Organic photolysis is assessed in GECKO-A via a lookup table of j-values for reference chromophores pre-calculated at different solar zenith angles with the TUV 1-D radiative transfer model (Madronich and Flocke, 1999). The reference cross-sections used in the model generally do not cover the UV wavelengths at which OFR operates (with narrow peaks at 185 nm and 254 nm) since they are not tropospherically relevant. Thus it was necessary to extend to 185 nm the relevant reference absorption cross-sections. We have done this using literature values via the Mainz UV-Vis spectral atlas (Keller-Rudek et al., 2020) or by extrapolating the available cross-section data, using other similar chromophores as references. Details of all cross-section extensions are given in Table S1. Where quantum yield information was not available, we assume values of unity since photons at 185 and 254 nm are usually sufficiently energetic to make photolysis occur (Ausloos and Lias, 1971). In case of multiple product channels for a photolyzed molecule, the branching ratios of those channels at 185 and 254 nm are estimated through extrapolation of branching ratio data from available ranges followed by a renormalization. Finally, we apply the OFR UV spectrum within TUV to calculate OFR-relevant j-value lookup tables.

2.2.3 Mechanism of low-NO m-xylene oxidation

The meta-xylene oxidation mechanism in GECKO-A follows MCM v3.2 until all aromatic, epoxy, or bridged-peroxy rings are broken (See Scheme S1). Since the MCM was designed for typical urban environments with abundant NO_x, it omits some reaction pathways for other oxidants, assuming them to be of negligible importance. The relevant photolysis loss pathways are slow under ambient conditions and inactive in the OFR case. This leads to persistence and accumulation of certain hydroperoxides and their interconverting peroxy radicals under low-NO conditions. We added two low-NO oxidation reactions to the xylenol branch of the meta-xylene oxidation scheme, Scheme S1. In the 51% branch, we allow the unsaturated bicyclic peroxide "MXYLOOH" to react with, sequentially, OH (estimating $k_{VOC+OH} \sim 3e^{-11}$ cm^3 molecule^{-1} s^{-1}) and HO$_2$ (estimating $k_{RO2+HO2} \sim 1e^{-11}$ cm^3 molecule^{-1} s^{-1}), to produce a saturated bicyclic peroxide (denoted "TT8001" in Scheme S1). In the 42% branch, we add a competing O_3 reaction with the alkoxy radical "MXCATEC1O", producing an unsaturated carbonyl alkoxy radical "1T8000" which eliminates CH3 to form the unsaturated cyclic hydroxy dicarbonyl "TU7000". Both products are then further oxidised via the standard GECKO SARs.

2.3 GECKO Loader and Plotter

To allow GECKO-A outputs, which are usually highly complex and voluminous, to be explored and visualized in detail on standard (non-UNIX) personal computers, we have developed the GECKO Loader and Plotter based in the data-analyzing and graphic-making package Igor Pro 8.0 (WaveMetrics, Lake Oswego, Oregon, USA). This tool assists on the rapid and detailed analysis of model-chamber/OFR

269 comparison studies.

270 Specifically, the GECKO Loader and Plotter facilitates: i) filtering the (sometimes extremely large
271 and finely-resolved) model results time series to examine specific characteristics, ii) identifying the most
272 abundant and/or influential species in each phase (gas, particle, and wall), iii) selecting species by
273 specific chemical identity (molecular formula, specific formula, and/or functional group identity), iv)
274 plotting time series of individual species and their formation/destruction rates, v) assessing and
275 displaying aggregated properties (volatility distribution, mass spectrum, Henry's law constant
276 distribution) of the product mixture and subsets thereof, and vi) calculating bulk characteristics of the
277 simulation (OH_{exp}, OHR_{VOC}, light intensity, elemental ratios etc.) and relating species abundances to
278 them.

279 **3   Results and discussions**

280 In this section, we will show the evolution of OHR_{VOC} in the photooxidation of different precursors
281 under various conditions. To aid the presentation of this evolution for larger precursors, whose
282 oxidation is more complex, the oxidation of the simplest VOC, i.e., methane, will be first discussed. After
283 presenting the results of individual precursors, we will compare the results between conditions and
284 between precursors to illustrate the general trends. Along with the OHR evolution, OH recycling ratio
285 (β_1, defined as number of OH molecules generated from organic reactions per OH consumed by
286 organics) and HO_x (= OH + HO_2) recycling ratio (β_2, defined as number of OH and HO_2 molecules
287 generated from organic reactions per OH consumed by organics) will also be discussed, as they are
288 important parameters that may considerably affect the budget of atmospheric oxidizing agents (Stone
289 et al., 2012) and the HO_2-to-OH ratio and RO_2 chemistry in OFR (Peng et al., 2015, 2019).

290 **3.1   Methane**

291 To explain one of the main features in the OHR evolution in VOC photooxidation, i.e., OHR_{VOC}
292 peaking at a certain OH_{exp}, the oxidation of CH_4 is employed as an example because of its simpler
293 mechanism (Scheme S2). The results of this oxidation under the ambient condition show that OHR_{VOC}
294 peaks at an OH_{exp} of about $1x10^{13}$ molecules cm^{-3} s (Fig. S3). As the OHR of the precursor always
295 decreases during its oxidation, the appearance of such a peak of OHR_{VOC} before all VOCs are finally
296 oxidized to CO_2 indicates that the OHR increase from intermediates and products is faster than the OHR
297 decrease of the precursor. This is obviously the case for CH_4 oxidation, as there is no significant CH_4 loss
298 before OH_{exp} ~ 10^{13} molecules cm^{-3} s by its very slow reaction with OH (rate constant on the order of
299 10^{-15} cm^3 $molecule^{-1}$ s^{-1}; Atkinson and Arey, 2003) and all the non-CO_2 intermediates/products of the
300 oxidation (CH_3OOH, CH_3OH, HCHO, and CO) are orders of magnitude more reactive toward OH than is
301 CH_4 (Atkinson and Arey, 2003). This large difference in precursor and intermediate/product oxidation
302 timescales allows the oxidations of intermediates/products (including CO, whose reaction rate constant
303 with OH is ~$2x10^{-13}$ cm^3 $molecule^{-1}$ s^{-1}; Burkholder et al., 2015) to establish a steady state, whereby the
304 OHR of the intermediates/products is proportional to the concentration/OHR of CH_4. After OH_{exp} ~ 10^{13}
305 molecules cm^{-3} s, CH_4 concentration decay, and consequently that of all intermediates/products,
306 become significant, giving the OHR_{VOC} peak around $1x10^{13}$ molecules cm^{-3} s.

307   We also performed a simulation under a typical OFR condition. The OHR_{VOC} peak also appears
308   around 1×10^{13} molecules cm^{-3} s in this case for the same reasons discussed above, but its height is
309   almost twice that of the ambient case (Fig. S3). The OHR of CO in both cases is similar, while that of
310   CH_3OH is higher in the ambient case but those of CH_3OOH and HCHO are significantly higher in the OFR
311   case. This is because the relative importance of the various reactions involved in CH_4 oxidation (Scheme
312   S2) depends on the conditions in each reactor.

313   In the OFR case, OH and HO_2 concentrations are ~4 and ~3 orders of magnitude higher than
314   typical ambient values, respectively (Peng et al., 2015). The reactions of two intermediates, CH_3OOH
315   and HCHO, with OH and the reaction of the only major RO_2 involved, CH_3OO, with HO_2 are much faster
316   than their photolysis or the self-reaction of CH_3OO (Scheme S2). Neglecting organic photolysis and
317   CH_3OO self-reaction (and thus CH_3OH as a product of the latter), the mechanism of CH_4 oxidation can
318   be simplified to an OH-driven chain ($CH_4 \rightarrow CH_3OOH \rightarrow HCHO \rightarrow CO \rightarrow CO_2$) with a fast steady-state
319   branch on CH_3OOH ($CH_3OOH \leftrightarrow CH_3OO$). For a simple chain, as we show in Appendix A, the OHR of
320   precursor and that of each intermediate are equal. At the OHR_{VOC} peak, the OHR of HCHO and CO are
321   very close to that of CH_4, while that of CH_3OOH is larger, because the branch reaction $CH_3OOH + OH \rightarrow$
322     $CH_3OO + H_2O$ also contributes to OHR, but does not affect the chain (and hence the OHR of the
323   downstream species). With such an idealized chain mechanism, the OHR_{VOC} peak height equals the
324   precursor OHR multiplied by the number of steps needed to produce CO_2.

325   In contrast, the OHR_{VOC} peak height (and its composition) in the ambient case cannot be
326   explained by the simple chain. Both HCHO photolysis and CH_3OO self-reaction play a major role in the
327   oxidation in this case, and are significantly faster than the reactions in the simple chain (HCHO + OH
328   and $CH_3OO + HO_2$). In terms of the relationship of these two reactions with the chain, HCHO photolysis
329   bypasses HCHO + OH in converting HCHO to CO, while CH_3OO self-reaction bypasses CH_3OOH, in effect
330   short-circuiting the involvement of OH in the oxidation and hence lowering OHR_{VOC} (Appendix A). Since
331   the only reaction of CO is CO + OH, its OHR at the OHR_{VOC} peak is essentially unaltered.

332 **3.2   Decane**

333 **3.2.1   Ambient and OFR cases**

334   The evolution of OHR_{VOC} during the oxidation of another alkane, decane, under ambient and OFR
335   conditions exhibit a smaller difference and smaller peak enhancements than those in the methane
336   cases (Fig. 1), although the chain lengths of the decane oxidation to CO_2 should be much longer than
337   that of methane. The ambient cases with constant and diurnal solar radiation have almost the same
338   OHR_{VOC} evolution as a function of OH_{exp} (Figs. 1 and 2).

339   These differences from the methane cases arise because a key assumption of the simple reaction
340   chain model, i.e., slow precursor decay allowing intermediates/products to build up and reach a steady
341   state, no longer holds in decane oxidation. The main first-generation products, i.e., secondary decyl
342   hydroperoxides, react with OH only less-than-3-times more rapidly (in terms of the rate constant of the
343   whole molecule) than does decane, as the significant activation effect of the –OOH group only applies
344   to the α-H, and all other H atoms in this long chain alkyl, though less reactive, can be abstracted by OH

345 (Kwok and Atkinson, 1995; Aumont et al., 2005). When decyl hydroperoxides are present in significant

346 amounts (OH_{exp} ~ $5x10^{10}$ molecules cm^{-3} s), decane loss is also significant (Fig. 3). Also, oxidation of

347 monohydroperoxides to ketones, their most likely fate (due to the activated α-H), lowers OHR_{VOC}, as

348 the oxidation removes the most activated H (Kwok and Atkinson, 1995). The multifunctional products

349 of further oxidation in the mid OH_{exp} range (before ~$2x10^{11}$ molecules cm^{-3} s), mainly have -OOH and -

350 CO- (Fig. 4), which do not further increase OHR substantially with respect to monohydroperoxides, for

351 similar reasons as the comparison of monohydroperoxides with decane. After the OHR_{VOC} peak, the

352 precursor is largely consumed and -CH(OOH)- groups become increasingly oxidized to -CO- in both

353 monohydroperoxides and multifunctional hydroperoxides (Figs. 3 and 4), which rapidly decreases

354 OHR_{VOC}. Since the decane oxidation chain does not reach a steady state, it results in only limited OHR_{VOC}

355 enhancement at peak.

356   In the absence of steady state for the nodes (stable species) in the decane oxidation chains

357 (nodes far downstream insufficiently populated), organic photolysis and RO_2 self- and cross-reactions

358 only help move OHR contributors to downstream nodes, but do not significantly change their total

359 concentrations. This is shown by the relatively small differences in the composition of stable OHR

360 contributors between the ambient and OFR cases (Fig. 3). The remarkable difference between these

361 cases is the contribution of RO_2 to OHR, which is as high as ~3 s^{-1} in the OFR case shown in Fig. 3, while

362 estimated to be only up to ~0.1 s^{-1} in the ambient case, given the RO_2 concentration in the simulation.

363   It is known that RO_2 + OH can be a significant RO_2 loss pathway in OFR, especially when OH and

364 HO_2 production is relatively strong (higher relative humidity (RH) and UV). We have previously advised

365 to avoid such conditions in low-NO chemistry based on simplified modeling, because of its high-NO-like

366 organic product (Peng et al., 2019). Here our chemically explicit modeling results show that the

367 limitation for OFR chemistry caused by RO_2 + OH may not be as serious as suggested by Peng et al.

368 (2019), at least in terms of OHR_{VOC} and, to some extent, of organic composition (Fig. 3). The condition

369 of the OFR case shown in Fig. 3 (30% RH, medium UV, and 10 s^{-1} initial OHR) is a compromise between

370 the goals of reaching an equivalent photochemical age of ~10 d, avoiding significant non-tropospheric

371 organic photolysis, and keeping a more atmospherically relevant RO_2 chemistry (Peng et al., 2016; Peng

372 et al., 2019; Peng and Jimenez, 2020). In this case, the fractional contribution of RO_2 + OH to RO_2 fate

373 is still sizable (>30%). However, the evolution of the composition of monofunctional species in this OFR

374 case before the OHR_{VOC} peak equivalent age is similar to that in the ambient case (Fig. 3), as

375 hydroperoxide production through RO_2 + HO_2 is still the main loss pathway of the first-generation RO_2

376 and RO produced from RO_2 + OH can also form ketones, i.e., the main second-generation products. The

377 other main fate of RO, i.e., isomerization, leads to slightly faster production of multifunctional species,

378 since the product of the recombination of the immediate product of this isomerization, i.e., an alkyl

379 radical, with O_2 is already a bifunctional RO_2. This isomerization also creates a hydroxyl group on the C

380 backbone, resulting in a relatively high share of hydroxyl in the functional groups of the multifunctional

381 species (Fig. 4).

382   Before the OHR_{VOC} peak, as OH_{exp} increases, carbonyls accumulate. They are prone to Norrish-

383 type photochemistry (Turro et al., 2009) which plays a major role in the OHR evolution after the OHR_{VOC}

384 peak in the ambient cases by breaking C10 species into smaller molecules (Fig. 3). Alkenes, which can

385 only be produced via Norrish Type II reaction in this case (Turro et al., 2009), are non-negligible OHR

386 contributors around 3×10^{11} molecules cm^{-3} s. A set of oxygenated C1 and C2 species are also largely

387 produced through organic photolysis followed by reactions with (O_2 and) HO_2. Organic photolysis, along

388 with OH reaction pathways, can also produce RO_2. Self- and cross-reactions of acylperoxy radicals,

389 which are formed in significant amounts in this OH_{exp} range, can rapidly generate alkoxy radicals

390 (Orlando and Tyndall, 2012), which may decompose subsequently (Ziemann and Atkinson, 2012). At

391 ~1×10^{12} molecules cm^{-3} s, the small species produced account for about half of OHR_{VOC} in the ambient

392 cases (Fig. 3). In the OFR cases, organic photolysis is usually much weaker than in the atmosphere (Peng

393 et al., 2016; Peng and Jimenez, 2020), as the negligible OHR of alkenes in the OFR case in Fig. 3 also

394 indicates. However, fragmentation of multifunctional species does not appear to be significantly

395 weaker in the OFR case than in the ambient case shown in Fig. 3. This is largely due to fast RO_2 + OH.

396 The reactions of acylperoxys with OH lead to direct fragmentation (Orlando and Tyndall, 2012). Highly

397 functionalized RO can also form from the reactions of multifunctional RO_2 with OH, and then often

398 rapidly decompose. RO_2 + OH also results in a major difference of the OFR case from the ambient case

399 at high equivalent ages (Fig. 3), i.e., lower (higher) OHR contribution from CH_3OOH (HCHO) in OFR than

400 in the atmosphere. Most CH_3OO reacts with OH to produce CH_3O then HCHO in the OFR case, leaving a

401 minor fraction of CH_3OO reacting with HO_2 to form CH_3OOH.

402 **3.2.2 Chamber cases**

403   Three types of chamber simulations, without gas-particle-wall partitioning, with gas-particle

404 partitioning only (no wall), and with gas-particle-wall partitioning, are considered in this study. The first

405 type has almost the same results as the ambient cases in terms of the evolution of OHRVOC and its

406 composition as a function of OH_{exp} (Fig. 1). Despite different spectra, sunlight and chamber lights cover

407 the same wavelength range and usually generate oxidizing agent radicals (e.g., OH and HO_2) in similar

408 amounts. Therefore, all key parameters are very similar between the ambient case with constant solar

409 radiation and the chamber case (with 10 s^{-1} initial OHR) and without gas-particle-wall partitioning. This

410 explains the high similarities between the results of the ambient cases and the chamber cases without

411 wall partitioning. Unfortunately, the lack of wall partitioning is not realistic for current chambers.

412   The chamber cases with gas-particle-wall partitioning at lower initial OHR, which are realistic,

413 show very large deviations from the ambient cases that cannot be explained by gas-particle partitioning

414 only (Figs. 1, 3 and S4). These deviations are mostly due to wall partitioning of OVOCs around the OH_{exp}

415 of the OHR peak and at lower OH_{exp}. In this OH_{exp} range, the wall removes about half of the OHR of

416 decane oxidation intermediates/products (Figs. 1 and 2) and hence also almost removes the OHRVOC

417 peak in the relevant chamber cases (Fig. 1). In detail, some decyl hydroperoxides partition to the wall

418 in the chamber case shown in Fig. 3, as decyl is a relatively large alkyl and leads to hydroperoxides of

419 sufficiently low volatility to promote wall partitioning. The C10 ketones, usually of higher volatility than

420 the corresponding hydroperoxides, do not show significant wall partitioning (Fig. 3), while about half of

421 the multifunctional C10 species, of even lower volatility than the corresponding hydroperoxides, are
422 partitioned to the wall.

423   At higher OH_{exp} (>2×10^{11} molecules cm^{-3} s), more multifunctional species stay in the gas phase
424 or partition to the particle phase (Figs. 3 and S4). Those in the gas phase are formed via C10
425 fragmentation and are thus of higher volatility (Fig. 3). Those partitioned to the particle phase instead
426 of the wall are due to a higher organic aerosol concentration resulting from accumulation during a long
427 oxidation. The substantial partitioning of multifunctional species to aerosol and the wall also slows
428 down their oxidative evolution in the gas phase relative to the ambient cases (Fig. 4). The degree of
429 oxidation of products partitioned to the particle phase increases since low OH_{exp}. This is due to a
430 volatility fractionation caused by the lower ability of the particle phase to absorb condensable organic
431 gases than that of the wall phase at this OH_{exp}. At low organic aerosol loading, the relative potential of
432 particle partitioning to wall partitioning for organic gases of higher functionalization is higher than for
433 those of lower functionalization.

434   At higher initial OHR (100 s-1), and hence higher organic aerosol loading, condensable gases
435 have a significantly higher tendency of partitioning to the particle phase. The reduction of OHR of the
436 higher initial OHR chamber case with aerosol partitioning only (no wall partitioning) relative to the
437 purely gas-phase case is comparable to the lower initial OHR case with gas-particle-wall partitioning at
438 low OH_{exp} (before the OHR peak) (Fig. S4). At high OH_{exp}, this OHR reduction is even stronger than in
439 the lower initial OHR case with gas-particle-wall partitioning, as partitioning of OVOCs to the particle
440 phase dominates over that to the walls.

441   As OH_{exp} increases and large multifunctional species are formed in increasing amounts from
442 oxidation, their substantial partitioning to aerosol and the wall decreases the OHR of decane oxidation
443 intermediates/products by a factor up to 8 around 1×1012 molecules cm-3 s compared to the chamber
444 cases without gas-particle-wall partitioning (Figs. 2 and S4). At higher OHexp (long oxidation times) gas-
445 phase concentrations of partitioning species decline, allowing reverse partitioning back from the
446 particle phase and the wall which then serves as a source rather than a sink. As a result, the ratio of the
447 OHR of oxidation intermediates/products in the chamber case with gas-particle-wall partitioning to that
448 without this partitioning decreases (Fig. 2).

449 **3.2.3 OH and HO_x recycling ratios**

450   As discussed above, we also compute OH (β_1) and HO_x (β_2) recycling ratios in decane oxidation.
451 Note that these quantities also include OH and HO_2 generated as a result of organic photolysis. The
452 differences in these recycling ratios between the simulated cases are relatively small. β_1 is close to 0 at
453 OH_{exp} < ~1×10^{10} molecules cm^{-3} s (Fig. 1), as the initial reaction of decane with OH only produces an RO_2
454 and subsequently C10 hydroperoxides, and no HO_x. Then β_1 undergoes a fast increase between ~1×10^{10}
455 and 1×10^{11} molecules cm^{-3} s (Fig. 1), as the further oxidation of C10 hydroperoxides to ketones fully
456 recycles OH (R_1-CH(OOH)-R_2 + OH → R_1-CO-R_2 + H_2O + OH) in the ambient and chamber cases.
457 Nevertheless, β_1 only increases up to ~0.4 at this stage in the ambient and chamber cases, as oxidation
458 of C10 hydroperoxides to dihydroperoxy species and precursor oxidation also account for a substantial

459   fraction of OH loss but do not recycle it. In the OFR cases, β_1 only increases up to ~0.2–0.3 at this stage,

460   since RO_2 + OH starts to be active but does not recycle OH. Then, β_1 roughly plateaus up to ~1×10^{12}

461   molecules cm^{-3} s, as the overall effect of the decrease in hydroperoxy concentration, reducing OH

462   recycling, and the increase in the concentration of acylperoxy, enhancing OH recycling through its

463   reaction with HO_2 (Orlando and Tyndall, 2012), is relatively small. Finally, β_1 gradually decreases to 0

464   (Fig. 1), as all OVOCs degrade to highly oxidized C1 species, i.e., HCHO, HCOOH, CO, which only have

465   HO_2 recycling but no OH recycling, and the unreactive CO_2.

466   The HO_x recycling ratio (β_2) in decane oxidation is similar to β_1 before ~1×10^{11} molecules cm^{-3} s

467   for the ambient and chamber cases, as only OH (but not HO_2) is recycled at this stage. β_2 is a little higher

468   in the OFR cases than in the other cases at this stage because of the HO_2 recycling by RO_2 + OH.

469   However, at higher OH_{exp}, β_2 continues to increase with OH_{exp} to a final value of 1 (Fig. 1). This difference

470   between β_1 and β_2 is by definition due to HO_2 recycling. Its significance rises in parallel with that of

471   organic photolysis, which can often produce HCO radicals and acylperoxy radicals. The former

472   extremely rapidly undergoes HCO + O_2 $\rightarrow$ CO + HO_2; the latter can rapidly convert peroxy radicals to

473   alkoxy radicals (Orlando and Tyndall, 2012), which may then react with O_2 to generate HO_2 (Ziemann

474   and Atkinson, 2012). At very high OH_{exp} (10^{12} – 10^{13} molecules cm^{-3} s), reactive highly oxidized small

475   VOCs are the dominant OHR contributors and many of them recycle HO_2 during their oxidation by OH

476   (Fig. 3). Finally, once CO becomes the only remaining OHR contributor, β_2 is 1.

477   **3.3   m-Xylene**

478   Most features in m-xylene oxidation can be explained based on similar discussions as for decane

479   oxidation in Section 3.2. OHR_{VOC} also has a maximum during the oxidation (Figs. 1 and S4), as most of

480   the direct products of m-xylene oxidation by OH, i.e., the unsaturated carbonyl (MXYEPOXMUC in MCM

481   v 3.2 notation, see Scheme S1), the unsaturated endo-cyclic peroxide (MXYBPEROOH), and xylenols,

482   are more reactive toward OH than m-xylene. The OHR of these initial products is enhanced much more

483   during the oxidation of m-xylene than of decane, owing to the creation of C=C bonds in many post-

484   aromatic (ring-opening) products, hence the OHR_{VOC} peak enhancement in m-xylene oxidation is larger

485   than in decane oxidation. Because the reaction rate constant of m-xylene with OH slightly exceeds that

486   of decane, the OHR_{VOC} peak in m-xylene oxidation occurs at slightly lower OH_{exp} than in decane

487   oxidation (Fig. 1). In the OFR case under the same condition as the decane case shown in Fig. 3, the

488   evolution of OHR of the stable organic species is again similar to that in the ambient case. And OHR_{VOC}

489   is higher in the OFR case again mainly due to OHR from RO_2 (Fig. 1 and S4). Several main first- and

490   second-generation products are already highly functionalized through fast O_2 addition (Scheme S1) and

491   they are also often unsaturated and prone to further functionalization. Therefore, the degree of

492   functionalization in saturated aliphatic multifunctional species is much higher in m-xylene than in

493   decane oxidation (Fig. 4). Also, as several aromatic-scheme-specific reaction types occur in the early

494   stages of m-xylene oxidation, e.g., endo O_2 addition (creating -OO- etc.) and ring-opening (creating -

495   CO-, -CHO etc.), multifunctional species functionality is more diverse than in decane oxidation (Fig. 4).

496   Photolysis again plays a role in species fragmentation and the production of highly oxidized C1 and C2

497 species after the OHR$_{VOC}$ peak (Fig. S4).

498 At low OH$_{exp}$ and that of the OHRVOC peak, particle and wall partitioning also substantially

499 reduces the OHRVOC in the relevant chamber cases of m-xylene oxidation while the OHRVOC reduction

500 due to partitioning to the particle phase is smaller than that due to the wall (Figs. 1, 2, S4 and S5). The

501 precursor (m-xylene) is a C8 species and even many first-generation products of its oxidation are highly

502 oxygenated (Scheme S1) lower-volatility species. The relative reduction of OHR of the

503 intermediates/products also increases with OH$_{exp}$ before the OH$_{exp}$ of the OHR peak, as volatile species

504 are oxidized and become more prone to wall partitioning (Figs. 2 and S4). At higher OH$_{exp}$, more

505 condensed organics are partitioned to the particle phase because of high organic aerosol concentration

506 (Fig. S4) and the wall and aerosol again serve as OVOC source (Fig. 2).

507 The evolution of β_1 and β_2 in m-xylene oxidation is somewhat different than in decane oxidation

508 (Fig. 1). In the ambient cases, they are non-negligible even at OH$_{exp}$ as low as 1×10^9 molecules cm^{-3} s

509 (~0.05 and ~0.45, respectively). OH is mainly recycled from one of endo-cyclic peroxide routes (m-

510 xylene + OH + 2O$_2$ $\rightarrow$ MXYBIPERO2; MXYBIPERO2 + HO$_2$ $\rightarrow$ MXYBPEROOH + O$_2$; MXYBPEROOH + OH $\rightarrow$

511 MXYOBPEROH + H$_2$O + OH (Scheme S1)), which involve various functional groups and open the

512 possibility of radical recycling. The third step of this route is very fast (with a rate constant on the order

513 of 10^{-10} cm^3 molecule^{-1} s^{-1}). Once the second step takes place, the third step contributes to OH recycling.

514 However, in the OFR cases with strong water vapor photolysis (not in the other OFR cases), the third

515 step does not play a significant role and β_1 is ~0 at very low OH$_{exp}$ (Fig. 1) due to the relatively slow

516 second step (RO$_2$ + HO$_2$). In the former cases, this is due to the relatively slow second step (RO$_2$ + HO$_2$),

517 while in the latter cases, the highly oxygenated compounds partition to the wall even more rapidly (in

518 hundreds of s; Krechmer et al., 2016) than their reactions with HO$_x$. Strong HO$_2$ recycling occurs in all

519 simulated cases from the beginning of the oxidation (Fig. 1), since two of the three major channels of

520 m-xylene + OH (i.e., those forming MXYEPOXMUC and xylenol, respectively) produce HO$_2$ as well.

521 As more multifunctional species are formed (particularly through ring-opening) near the OH$_{exp}$

522 of the peak OHR$_{VOC}$, HO$_x$ recycling is also active, with β_1 increasing and β_2 remaining high (Fig. 1). There

523 is a high peak in β_2 for the chamber case with high initial OHR (100 s^{-1}) and no aerosol or wall

524 partitioning. It results from RO$_2$ cross-reactions, many of which produce alkoxy radicals that

525 subsequently yield carbonyls and HO$_2$ through reactions with O$_2$ (Orlando and Tyndall, 2012). RO$_2$ cross-

526 reactions are significant in that OH$_{exp}$ range also because i) high precursor concentration translates into

527 higher RO2 concentration and ii) acylperoxy radicals, whose reactions with other RO$_2$ are fast (Orlando

528 and Tyndall, 2012), are rapidly formed from the oxidation of -CHO groups in the ring-opening products

529 (Scheme S1). The chamber case with high initial OHR and gas-particle-wall partitioning does not have

530 such a high β_2 peak, because of fast partitioning of the oxidation products containing -CHO groups to

531 the aerosol and wall phases, which significantly reduces acylperoxy radical concentration around the

532 OH$_{exp}$ of the peak OHRVOC. At higher OH$_{exp}$, calculated β_1 and β_2 become less reliable, since remaining

533 apparent OHR contributors may in fact be persistent artifacts of the incompleteness of the (hand-

534 written) m-xylene oxidation mechanism which may substantially bias β_1 and β_2 when the

535   concentrations of remaining OHR contributors should be generally low. Therefore, we do not try to

536   interpret the features in β_1 and β_2 at high OH_{exp} for m-xylene oxidation.

537   **3.4   Isoprene**

538   The most salient difference of the OHR_{VOC} evolution in the photooxidation of isoprene from that

539   of the other precursors in this study is the lack of OHR_{VOC} peak in the isoprene cases (Figs. 1 and S5).

540   The decrease in OHR_{VOC} all along this photooxidation is expected since the reaction of isoprene with OH

541   is very fast (at 1×10^{-10} cm^3 molecule^{-1} s^{-1}; Atkinson and Arey, 2003) and all intermediates/products of

542   this photooxidation react with OH more slowly than isoprene. The OHR_{VOC} of the

543   intermediates/products peaks slightly after an OH_{exp} of 1×10^{10} molecules cm^{-3} s (Fig. 1). At this OH_{exp},

544   the main type of the first-generation products, oxygenated unsaturated species (e.g., isoprene-derived

545   unsaturated hydroxyl hydroperoxides (ISOPOOH)), are largely produced from isoprene + OH and their

546   loss rates (with rate constant with OH slightly lower than that of isoprene) reach the maxima (Fig. S5).

547   Further oxidation leads to the loss of all C=C bonds in the isoprene C backbone and thus a substantial

548   drop of the OHR of the molecule.

549   Before $OH_{exp} \sim 5 \times 10^{10}$ molecules cm^{-3} s in isoprene photooxidation, the main deviations from the

550   ambient cases shown by the chamber cases with wall partitioning are again caused by wall partitioning

551   of multifunctional species, but their relative magnitudes are different than in the photooxidations of

552   decane and m-xylene, with the impacts of wall partitioning being smaller (Fig. S5). Oxygenated species

553   derived from isoprene, a C5 species, should be generally more volatile and less prone to wall

554   partitioning than those derived from decane and m-xylene. On the other hand, isoprene reacts with OH

555   much more rapidly than do decane or m-xylene, creating a larger deviation from the steady state for

556   RO_2 directly derived from isoprene and a more remarkable decrease in the OHR of the first-generation

557   products (Fig. S5). In the OFR case shown in Fig. S5, RO_2 contributes negligibly to OHR_{VOC}, since many

558   first-generation isoprene-derived RO_2 have other very fast loss pathways and the very fast decay of

559   isoprene cannot sustain RO_2 production at $OH_{exp} > \sim 1 \times 10^{10}$ molecules cm^{-3} s.

560   After $OH_{exp} \sim 5 \times 10^{10}$ molecules cm-3 s, the deviation caused by chamber wall partitioning

561   becomes more significant as highly oxidized and lower-volatility multifunctional species (Fig. 4) are

562   formed in significant amounts (Figs. 2 and S6). However, aerosol partitioning does not become more

563   significant as in the chamber cases of isoprene oxidation aerosol formation is always so small that

564   partitioning to the particle phase never competes with that to the walls. At very high OH_{exp}, the wall

565   again acts as a source of OVOCs in isoprene oxidation, as in those of the other precursors (Fig. 2). The

566   deviations of OFR cases from the ambient cases are mainly caused by RO_2 + OH and lack of organic

567   photolysis. These two effects lead to too much HCHO produced and inefficient production of other C1

568   and C2 species (Fig. S5).

569   To test whether one of the issues, i.e., lack of organic photolysis in OFR, can be mitigated by

570   adding tropospherically-relevant UV sources, we perform two additional simulations. Adding the

571   emissions corresponding to high Hg lamp setting with five times the UV of the CU Chamber (a rough

572   upper limit for experimental implementation) has negligible effect (Fig. S6). To reach a ratio between

573 tropospherically-relevant UV (UVA+UVB) intensity and OH concentration similar to that in the ambient

574 case with constant sunlight requires addition of a chamber light ~10000 times stronger than the CU

575 Chamber light. Such a strong UV source is obviously not realistic, and, while it does increase both early

576 organic photolysis and the relative contribution of C1 and C2 photoproducts to OHR_{VOC} around 2×10^{11}

577 molecules cm^{-3} s (Fig. S6), it increases the deviation of this OFR case from the ambient cases at very

578 high OH_{exp}, where oxidation of C1 and C2 species to CO proceeds much more rapidly than in the

579 atmosphere.

580 Product functionality in isoprene oxidation is more diverse than in decane oxidation (Fig. 4). This

581 is due to both the propensity of the isoprene C=C bonds to addition of various groups, and the active

582 isomerization of isoprene oxidation intermediates (Wennberg et al., 2018). Notably, epoxy groups in

583 species such as isoprene-derived epoxydiol (IEPOX) account for a large fraction of saturated product

584 functionality (Fig. 4), particularly at OH_{exp} on the order of 10^{10} molecules cm^{-3} s. In the gas phase of the

585 chamber cases with wall partitioning, the overwhelming majority of saturated multifunctional organic

586 molecules are IEPOX up to 1×10^{11} molecules cm^{-3} s (Fig. 4), as more highly-oxidized species mostly

587 partition to the wall.

588 IEPOX formation from isoprene-derived hydroperoxide (ISOPOOH) oxidation by OH (ISOPOOH +

589 OH $\rightarrow$ IEPOX + OH) leads to the peak of OH recycling around 3×10^{10} molecules cm^{-3} s (Fig. 1). OH

590 recycling is active even at very low OH_{exp} (1×10^{9} molecules cm^{-3} s) because a significant amount of

591 ISOPOOH forms early and can recycle OH through its oxidation, except in the OFR cases with strong

592 water vapor photolysis, where ISOPOOH cannot be efficiently formed from first-generation RO_2. HO_2

593 recycling is also active in the entire course of the photooxidation (Fig. 1), because of a number of

594 isomerization and photolysis pathways that form alkoxy radicals and highly oxidized C1 species such as

595 HCOOH, HCHO, and CO at very high OH_{exp} (Fig. S5).

596 **3.5   Trends in OHR per C atom**

597 To explore some general trends of OHR evolution in VOC photooxidation, simulations are

598 performed for the ambient cases with constant UV for two additional alkanes between methane and

599 decane, i.e., butane and heptane. The results of these simulations are compared to the existing

600 analogous cases in Fig. 5. For all cases, the OHR_{VOC} peak height decreases and the OH_{exp} of the OHR_{VOC}

601 peak shifts towards lower OH_{exp}, as the C number of the precursor alkane increases. This can be

602 explained by the fact that the OH rate constants of these alkanes increase with C number, and suggests

603 a possible general trend between OHR peak location and C number.

604 To explore these trends further, we calculate the OHR per unit starting concentration of C atom

605 (in the precursor) in all ambient cases with constant UV in this study (Fig. 5b). In this study, CO_2 is not

606 included initially but produced during the oxidation. Therefore, C atoms in the produced CO_2 are taken

607 into account in the calculation of OHR per C atom. For real atmospheric cases, initial CO_2 is present but

608 should not be considered in this calculation. Note that OHR per C atom has a unit of cm^3 $atom^{-1}$ s^{-1} and

609 represents the average contribution to the rate constant with OH of all considered C atoms. Despite

610 large differences among the reactivities of these precursors, the OHR per C atom in the simulations of

611   all precursors but methane converges near an OH_{exp} of $3x10^{11}$ molecules cm^{-3} s, and then follows a very

612   similar downward trend (Fig. 5b). This OH_{exp} value is roughly where saturated multifunctional species

613   have their maximal relative contribution to the OHR_{VOC} (Figs. 3 and S5). Even in the ambient cases of m-

614   xylene oxidation, saturated multifunctional species also account for about half of OHR_{VOC} when the

615   contribution of aromatics, some of which may artificially persist due to mechanism incompleteness, is

616   excluded (Fig. S4). Also, at OH_{exp} > ~$3x10^{11}$ molecules cm^{-3} s, a C atom in saturated multifunctional

617   species on average has at least 0.3 functional groups in the ambient cases (Fig. 4), and the functional

618   group composition is relatively diverse at this OH_{exp}. Therefore, the convergence value of OHR per C

619   atom of ~$2x10^{-12}$ cm^3 $atom^{-1}$ s^{-1} at ~$3x10^{11}$ molecules cm^{-3} s can be largely regarded as a relatively

620   invariant average of those of secondary H and α-H of various O-containing functional groups. Note that

621   this average is for low-NO conditions and can be lower at high NO due to deactivating effects of N-

622   containing groups formed during oxidation (Isaacman-VanWertz and Aumont, 2021).

623   Before the convergence, isoprene has the highest OHR per C atom (on the order of 10^{-11} cm^3

624    $atom^{-1}$ s^{-1}) among the precursors and intermediates/products (Fig. 5b), because of its conjugated C=C

625   bonds. The OHR per C atom of its first-generation oxidation products is slightly lower and close to that

626   of the oxidation intermediates/products of m-xylene, as the main contributors in both cases are

627   oxygenated monoalkenes. The average OHR per C atom of the studied alkanes increases with C number

628   (Fig. 5b), with the upper limit around $1x10^{-12}$ cm^3 $atom^{-1}$ s^{-1} consistent with Kwok and Atkinson (1995),

629   since the less-reactive -CH_3 groups (with OHR per C atom of ~$1x10^{-13}$ cm^3 $atom^{-1}$ s^{-1}) contribute

630   proportionally less to molecular OHR as C number increases. Conversely, the early-stage products of

631   alkane oxidation (mainly alkyl monohydroperoxides) show higher average OHR per C atom for shorter

632   molecules (Fig. 5b), owing to the activating (increasing OHR) contribution of the -OOH group.

633   Following the convergence of OHR per C atom, this quantity in all non-methane ambient cases

634   in this study sees a similar decay (Fig. 5b). This coincides with multifunctional species broken into small

635   highly oxidized C1 and C2 compounds. Although among them there are species with OHR per C atom >

636    $5x10^{-12}$ cm^3 $atom^{-1}$ s^{-1} (e.g., CH_3OOH, CH_3CHO, and HCHO), the average OHR per C atom of these C1 and

637   C2 species are mainly governed by those reacting more slowly (e.g., HCOOH and particularly CO) and

638   hence reaching higher concentrations amid the fast decay of multifunctional species. The similar fast

639   drop of OHR per C atom after OH_{exp}~$1x10^{12}$ molecules cm^{-3} s for various precursors implies a transition

640   from OHR from saturated multifunctional molecules to OHR from CO before the final oxidation to CO_2

641   (which has zero OHR).

642   **3.6   Total OH consumption for each precursor**

643   Integrating OHR per C atom over OH_{exp} allows us to assess the average number of OH molecules

644   consumed by each C atom during the entire course of oxidation. This quantity can also be apportioned

645   to the contributions of different OH reactants (Fig. 6). Due to incomplete oxidation of several species,

646   especially CO, the value of this quantity for an oxidation with all C atoms ending up with CO_2 should be

647   higher than those at simulation end (OH_{exp}~$4x10^{12}$ molecules cm^{-3} s). We correct this in Fig. 6 by

648   including additional contribution of CO to make its total contribution 1, since CO, the typical

649 penultimate product, consumes one OH molecule in its final oxidation, but is still present in significant

650 quantities at the end of our simulations. Thus, each C atom reacts with OH ~3 times in the course of the

651 oxidation of isoprene and decane to CO_2 (Fig. 6). A simplistic and chemically intuitive explanation for

652 this number is that the average oxidation state ($\overline{OS_C}$) of both isoprene and decane C atoms is ~-2, and

653 needs to increase to the value of +4 in CO_2 at the end of the oxidation. A C1 unit reacting once with OH

654 likely increases its $\overline{OS_C}$ by ~2. This increase is usually realized by an abstraction of H atom by OH or an

655 addition of OH ($\overline{OS_C}$+ 1), followed by an abstraction of H atom by O_2 or an addition of O_2 ($\overline{OS_C}$+ 1). Note

656 that ~3 OH consumed per C atom oxidized to CO_2 is likely an upper limit, since the mechanisms in this

657 study do not include RO_2 autoxidation (Crounse et al., 2013; Ehn et al., 2014), which reduces the

658 number of OH needed for complete VOC oxidation. Also, in a real low-NO environment, NO is still

659 present in low concentrations and converts RO_2 to RO. RO may undergo H abstraction through

660 isomerization or reaction with O_2, which also lowers the number of OH needed, although the effect is

661 usually small. The number of OH consumed per C atom in m-xylene oxidation is slightly lower than 3

662 (Fig. 6) because of the multiple addition of O_2 following a single OH addition in the initiation reaction,

663 i.e., m-xylene + OH.

664 **4   Summary and conclusions**

665 Using the fully explicit GECKO-A model, we simulated OHR evolution in the photooxidation of

666 several types of VOCs (i.e., alkane, alkene, and aromatic) without NO until very high equivalent

667 photochemical ages (>10 d) under a variety of conditions (in the atmosphere, chamber, and OFR). We

668 analyzed the simulations in detail and found a number of common features as well as some differences

669 resulting from certain precursors. These features are summarized below:

670 -   All simulated non-methane cases very roughly follow this general oxidation chain pattern: precursor

671   → first-generation products → (second-generation products →) multifunctional species → highly

672   oxidized C1 and C2 species → CO (or HCOOH) → CO_2. These species are generally not at steady

673   state and gain significance/predominance one after another in the entire course of oxidation.

674   Simulation results suggest that fragmentation products are not formed in significant amounts until

675   the late stage of the oxidation, which would be a key difference from studies of OHR evolution in

676   high-NO VOC oxidation (Nakashima et al., 2012; Sato et al., 2017).

677 -   In methane oxidation, the intermediates do not gain dominance in sequence. Instead, they

678   simultaneously increase as the oxidation proceeds, then simultaneously decrease when the

679   methane decay becomes significant. The OHR evolution in methane oxidation is close to the

680   idealized steady-state chain model, as the reaction of methane with OH is orders of magnitude

681   slower than those of its oxidation intermediates, which allows the intermediates to reach their

682   steady state.

683 The following discussion refers to the non-methane cases.

684 -   Where different types of species dominate OHR_{VOC} in sequence, OHR_{VOC} increases after the current

685   dominant type converts to one with a higher average OHR per C atom, and vice versa.

686   Photooxidations of alkanes and aromatics follow the increasing trend from precursor to saturated

687 multifunctional species (via alkyl monohydroperoxides) and from precursor to unsaturated
688 oxygenated species, respectively. The increase in aromatic oxidation is likely to be more significant,
689 since unsaturated oxygenated species are more reactive than saturated multifunctional species.
690 The conversions from multifunctional species to CO_2 lead to a decay of OHR_{VOC} in both alkane and
691 aromatic photooxidations. OHR_{VOC} in alkene photooxidation is likely to always drop rapidly during
692 C=C bond oxidation and more slowly afterwards.

693 - A relatively weak enhancement of OHR per C atom of a C atom with -OOH substitution can explain
694 the large range spanned by the precursors and their intermediates/products in this study at low
695 OH_{exp}. Around an OH_{exp} of 3×10^{11} molecules cm^{-3} s, precursors are largely converted to saturated
696 multifunctional species (e.g., by addition to C=C bonds in unsaturated precursors and abstraction
697 of H atoms in saturated precursors), and the reactive mixtures of those precursors thus have similar
698 OHR per C atom. They then all follow the course: multifunctional species → highly oxidized C1 and
699 C2 species → CO (or HCOOH) → CO_2 and show similar decays of OHR per C atom.

700 - In decane and isoprene oxidation, our simulations show that each C atom consumes at most ~3 OH
701 molecules in the course of its oxidation to CO_2. This can be simplistically explained as 3 occurrences
702 of oxidation by OH that increase, by 2 each time, the $\overline{OS_C}$ of decane and isoprene (~-2) to that of
703 CO_2 (+4). The total number of OH consumed by each C atom is likely to be lower when RO_2
704 autoxidation can be included in the mechanism generation.

705 In general, the OHR evolution differences resulting from different precursors are larger than those due
706 to different conditions. The difference in OHR_{VOC} between the ambient cases with constant and
707 diurnal sunlight is small. Nevertheless, physical conditions may still lead to significant differences,
708 which are summarized below:

709 - In current chambers, gas-wall partitioning can be a prominent issue that causes substantial wall
710 partitioning of certain OVOCs of lower volatility, depending on the chemical system under study.
711 The clearest example in this study is the substantial wall losses of C10 multifunctional species from
712 the gas phase in decane oxidation, and hence the remarkably lowered OHRVOC peak height in the
713 chamber simulation. The wall also preferentially absorbs more oxidized (and thus lower-volatility)
714 species, which alters the functional composition of gas-phase multifunctional species. The wall can
715 even serve as a source of multifunctional species at very high OH_{exp}, when the gas-phase
716 concentrations of those species are very low. The magnitude of the effects of wall partitioning also
717 depends on the size of the precursor, with the oxidation of larger precursors in chambers suffering
718 larger impacts of wall partitioning.

719 - The strong wall losses have important implications, as they can change our modeling results
720 substantially. Systematic OVOC gas-particle-wall partitioning corrections must be made for low-NO
721 oxidation chamber experiments that study OHR_{VOC}. In case of large precursors, highly chemically
722 explicit modeling will likely be necessary to infer the OHR of multifunctional species, which may
723 account for a large fraction of missing reactivity but suffer substantial wall losses. Although the few
724 existing chamber studies on OHR_{VOC} evolution were all under high-NO conditions, which may result

725   in more fragmentation and higher-volatility products, the magnitude of wall partitioning of large

726   multifunctional species in this study is so substantial that we believe this effect would also be

727   important at high NO. Schwantes et al. (2017) considered wall partitioning in their modeling of o-

728   cresol oxidation based on MCM v3.3.1 but still could not achieve good agreement with the

729   measurements for a number of products. Considering this, one should not assume that it is

730   appropriate to neglect gas-particle-wall partitioning in high-NO chamber experiments, just based

731   on agreement between the high-NO chamber experiments and modeling with MCM-based

732   schemes and without gas-particle-wall partitioning corrections. Even for OHR studies with less

733   surface loss issues, e.g., ambient studies, a combination of gas-phase-only OHR measurement and

734   modeling may still not be adequate as reduction of OHR due to OVOC condensation on aerosols can

735   also be significant in some situations (Fig. S4). Therefore, condensed phases (particle and wall) need

736   to be included in future OHR studies to better assess the deviation of the actual OHR from a purely

737   gas-phase picture.

738   -   OFR has two issues under certain conditions that can cause deviations from the ambient cases in

739   terms of OHR_{VOC}. Strong RO_2 + OH may significantly contribute to OHR_{VOC}. Interestingly, this type of

740   reaction does not seem to be able to substantially alter the composition of OHR_{VOC}. before the

741   OHR_{VOC} peak. Besides, the conditions resulting in strong water vapor photolysis have already been

742   identified as those leading to atmospherically irrelevant RO_2 chemistry in low-NO OFR in previous

743   studies (Peng et al., 2019; Peng and Jimenez, 2020). As long as OFR users follow the guidelines for

744   experimental planning provided in those studies (and use a much lower UV lamp setting), strong

745   RO_2 + OH can be avoided, as shown in Fig. 1.

746   -   The other main issue of OFR is lack of efficient organic photolysis, particularly at high OH_{exp}, when

747   multifunctional species break into highly oxidized C1 and C2 compounds. This problem has been

748   highlighted in previous studies (Peng et al., 2016; Peng and Jimenez, 2020) and been shown again

749   in the present work to be extremely difficult to avoid if a high OH_{exp} is desired. However, the

750   conversion of multifunctional species into highly oxidized C1 and C2 species may not be much

751   slower in OFR than in the atmosphere, since RO_2 + OH, leading to RO formation and subsequently

752   its decomposition, may also play a major role in this conversion. This also results in significantly

753   higher (lower) production of HCHO (CH_3OOH) in OFR than in the atmosphere at high equivalent

754   ages.

755   With all the key findings in this study presented above, we believe that we have, to some extent,

756   addressed the issues of "missing reactivity", of model limitations, and of OHR in remote areas for OHR

757   studies raised by Williams and Brune (2015). With the fully explicit GECKO-A model, we speciated the

758   likely source of the "missing reactivity", i.e., multifunctional OVOCs. A contrast between the technical

759   issues in some isoprene and m-xylene simulations and the high consistency in the other cases highlights

760   the importance of the completeness of the mechanism (even beyond the MCM level) in OHR-related

761   modeling studies. Substantial wall partitioning of OVOCs in some chamber experiments highlights the

762   importance of better constraining "gas-to-surface deposition terms''. More studies, both modeling

763 (with highly chemically explicit mechanisms) and experimental (particularly low-NO), are needed to

764 achieve better model-experiment closure. Finally, this study may have opened up the possibility of

765 parameterizing the OHR evolution in (at least low-NO) VOC photooxidation as a function of OH_{exp} only

766 with the often-available knowledge on the first- and second-generation products and the relevant SARs

767 such as Kwok and Atkinson (1995), as the OHR evolution beyond multifunctional species has been

768 shown to be similar for most VOC oxidations. This parametrization may be utilized in regional and global

769 models to better constrain OHR at high equivalent photochemical ages, e.g., in remote regions.

770

771 **Appendix A: The effect on OH reactivity of non-OH reactions in an OH-driven reaction chain**

772 1)   Consider the following reaction chain, where OH is the only oxidant:

773 $A_1 + OH \rightarrow A_2$, k_1

774 $A_2 + OH \rightarrow A_3$, k_2

775 $A_3 + OH \rightarrow A_4$, k_3
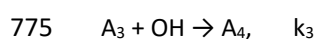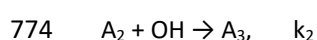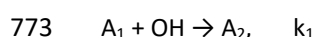
776 ...(etc.)

777 At steady state, $k_1[A_1][OH] = k_2[A_2][OH] = k_3[A_3][OH] = ... = C$ (C is a constant).

778 Then OHR due to individual species, OHR_i, is equal to $C/[OH]$ and is identical for all species.

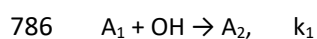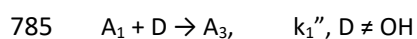779 2)   Consider a parallel conversion of A_1 to A_2 by a means other than reaction with OH:

780 $A_1 + OH \rightarrow A_2$, k_1

781 $A_1 + B \rightarrow A_2$, k_1', $B \neq OH$
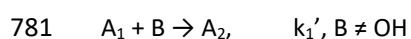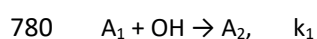
782 At steady state, $k_1[A_1][OH] + k_1'[A_1][B] = C$.

783 Therefore, $OHR_{A1} = k_1[A_1] < C/[OH]$.

784 3)   Now consider a reaction converting A_1 directly to A_3 occurring in parallel to reaction chain 1),

785 $A_1 + D \rightarrow A_3$, k_1'', $D \neq OH$

786 $A_1 + OH \rightarrow A_2$, k_1

787 $A_2 + OH \rightarrow A_3$, k_2
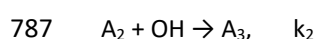
788 At steady state, $k_1''[A_1][D] + k_2[A_2][OH] = C$

789 And $OHR_{A1} < C/[OH]$, since $k_1[A_1][OH] = k_2[A_2][OH]$.

790

791 **Code/Data availability**

792 The chemical mechanisms generated and the outputs of the GECKO-A simulations in this study are
793 available upon request.

794

795 **Author contribution**

796 ZP and JLJ conceived the study. ZP designed the study. JL-T and ZP performed the simulations. HS, JL-T,
797 ZP, and JLJ developed the GECKO Loader and Plotter. ZP, JL-T, JJO, and BA made updates and
798 developments for GECKO-A. ZP, JL-T, JJO, BA, and JLJ analyzed the results. ZP led the manuscript writing
799 with inputs from all authors.

800

801 **Conflicts of interest**

802 There are no conflicts to declare.

803

Acknowledgements

809

810 **References**

811 Atkinson, R. and Arey, J.: Atmospheric Degradation of Volatile Organic Compounds, Chem. Rev.,
812 103(12), 4605–4638, doi:10.1021/cr0206420, 2003.

813 Aumont, B., Szopa, S. and Madronich, S.: Modelling the evolution of organic carbon during its gas-phase
814 tropospheric oxidation: development of an explicit model based on a self generating approach, Atmos.
815 Chem. Phys., 5(9), 2497–2517, doi:10.5194/acp-5-2497-2005, 2005.

816 Ausloos, P. J. and Lias, S. G.: Photochemistry in the Far Ultraviolet, Annu. Rev. Phys. Chem., 22(1), 85–
817 107, doi:10.1146/annurev.pc.22.100171.000505, 1971.

818 Bloss, C., Wagner, V., Jenkin, M. E., Volkamer, R., Bloss, W. J., Lee, J. D., Heard, D. E., Wirtz, K., Martin-
819 Reviejo, M., Rea, G., Wenger, J. C. and Pilling, M. J.: Development of a detailed chemical mechanism
820 (MCMv3.1) for the atmospheric oxidation of aromatic hydrocarbons, Atmos. Chem. Phys., 5(3), 641–
821 664, doi:10.5194/acp-5-641-2005, 2005.

822 Brune, W. H.: The Chamber Wall Index for Gas–Wall Interactions in Atmospheric Environmental
823 Enclosures, Environ. Sci. Technol., 53(7), 3645–3652, doi:10.1021/acs.est.8b06260, 2019.

824 Burkholder, J. B., Sander, S. P., Abbatt, J., Barker, J. R., Huie, R. E., Kolb, C. E., Kurylo, M. J., Orkin, V. L.,
825 Wilmouth, D. M. and Wine, P. H.: Chemical Kinetics and Photochemical Data for Use in Atmospheric
826 Studies: Evaluation Number 18, Pasadena, CA, USA. [online] Available from:
827 http://jpldataeval.jpl.nasa.gov/, 2015.

828 Camredon, M., Aumont, B., Lee-Taylor, J. and Madronich, S.: The SOA/VOC/NOₓ system: an explicit
829 model of secondary organic aerosol formation, Atmos. Chem. Phys., 7(21), 5599–5610,
830 doi:10.5194/acp-7-5599-2007, 2007.

831 Chameides, W., Lindsay, R., Richardson, J. and Kiang, C.: The role of biogenic hydrocarbons in urban
832 photochemical smog: Atlanta as a case study, Science (80-.)., 241(4872), 1473–1475,
833 doi:10.1126/science.3420404, 1988.

834 Crounse, J. D., Nielsen, L. B., Jørgensen, S., Kjaergaard, H. G. and Wennberg, P. O.: Autoxidation of
835 organic compounds in the atmosphere, J. Phys. Chem. Lett., 4, 3513–3520, doi:10.1021/jz4019207,
836 2013.

837 Ehn, M., Thornton, J. a, Kleist, E., Sipilä, M., Junninen, H., Pullinen, I., Springer, M., Rubach, F., Tillmann,
838 R., Lee, B., Lopez-Hilfiker, F., Andres, S., Acir, I.-H., Rissanen, M., Jokinen, T., Schobesberger, S.,
839 Kangasluoma, J., Kontkanen, J., Nieminen, T., Kurtén, T., Nielsen, L. B., Jørgensen, S., Kjaergaard, H. G.,
840 Canagaratna, M., Maso, M. D., Berndt, T., Petäjä, T., Wahner, A., Kerminen, V.-M., Kulmala, M.,
841 Worsnop, D. R., Wildt, J. and Mentel, T. F.: A large source of low-volatility secondary organic aerosol,
842 Nature, 506(7489), 476–479, doi:10.1038/nature13032, 2014.

843 Cohen, A. J., Brauer, M., Burnett, R., Anderson, H. R., Frostad, J., Estep, K., Balakrishnan, K., Brunekreef,
844 B., Dandona, L., Dandona, R., Feigin, V., Freedman, G., Hubbell, B., Jobling, A., Kan, H., Knibbs, L., Liu,
845 Y., Martin, R., Morawska, L., Pope, C. A., Shin, H., Straif, K., Shaddick, G., Thomas, M., van Dingenen, R.,
846 van Donkelaar, A., Vos, T., Murray, C. J. L. and Forouzanfar, M. H.: Estimates and 25-year trends of the
847 global burden of disease attributable to ambient air pollution: an analysis of data from the Global
848 Burden of Diseases Study 2015, Lancet, 389(10082), 1907–1918, doi:10.1016/S0140-6736(17)30505-6,
849 2017.

850 Fuchs, H., Hofzumahaus, A., Rohrer, F., Bohn, B., Brauers, T., Dorn, H. P., Haseler, R., Holland, F.,
851 Kaminski, M., Li, X., Lu, K., Nehr, S., Tillmann, R., Wegener, R., and Wahner, A.: Experimental evidence
852 for efficient hydroxyl radical regeneration in isoprene oxidation, Nature Geoscience, 6, 1023-1026,
853 doi:10.1038/Ngeo1964, 2013.

854 Fuchs, H., Novelli, A., Rolletter, M., Hofzumahaus, A., Pfannerstill, E. Y., Kessel, S., Edtbauer, A.,
855 Williams, J., Michoud, V., Dusanter, S., Locoge, N., Zannoni, N., Gros, V., Truong, F., Sarda-Esteve, R.,
856 Cryer, D. R., Brumby, C. A., Whalley, L. K., Stone, D., Seakins, P. W., Heard, D. E., Schoemaecker, C.,
857 Blocquet, M., Coudert, S., Batut, S., Fittschen, C., Thames, A. B., Brune, W. H., Ernest, C., Harder, H.,
858 Muller, J. B. A., Elste, T., Kubistin, D., Andres, S., Bohn, B., Hohaus, T., Holland, F., Li, X., Rohrer, F.,
859 Kiendler-Scharr, A., Tillmann, R., Wegener, R., Yu, Z., Zou, Q. and Wahner, A.: Comparison of OH
860 reactivity measurements in the atmospheric simulation chamber SAPHIR, Atmos. Meas. Tech., 10(10),

861 4023–4053, doi:10.5194/amt-10-4023-2017, 2017.

862 George, I. J. and Abbatt, J. P. D.: Heterogeneous oxidation of atmospheric aerosol particles by gas-phase
863 radicals., Nat. Chem., 2(9), 713–22, doi:10.1038/nchem.806, 2010.

864 Haagen-Smit, A. J.: Chemistry and Physiology of Los Angeles Smog, Ind. Eng. Chem., 44(6), 1342–1346,
865 doi:10.1021/ie50510a045, 1952.

866 Hallquist, M., Wenger, J. C., Baltensperger, U., Rudich, Y., Simpson, D., Claeys, M., Dommen, J.,
867 Donahue, N. M., George, C., Goldstein, A. H., Hamilton, J. F., Herrmann, H., Hoffmann, T., Iinuma, Y.,
868 Jang, M., Jenkin, M. E., Jimenez, J. L., Kiendler-Scharr, A., Maenhaut, W., McFiggans, G., Mentel, T. F.,
869 Monod, A., Prevot, A. S. H., Seinfeld, J. H., Surratt, J. D., Szmigielski, R. and Wildt, J.: The formation,
870 properties and impact of secondary organic aerosol: current and emerging issues, Atmos. Chem. Phys.,
871 9(14), 5155–5236, 2009.

872 Hodzic, A., Campuzano-Jost, P., Bian, H., Chin, M., Colarco, P. R., Day, D. A., Froyd, K. D., Heinold, B., Jo,
873 D. S., Katich, J. M., Kodros, J. K., Nault, B. A., Pierce, J. R., Ray, E., Schacht, J., Schill, G. P., Schroder, J. C.,
874 Schwarz, J. P., Sueper, D. T., Tegen, I., Tilmes, S., Tsigaridis, K., Yu, P. and Jimenez, J. L.: Characterization
875 of organic aerosol across the global remote troposphere: a comparison of ATom measurements and
876 global chemistry models, Atmos. Chem. Phys., 20(8), 4607–4635, doi:10.5194/acp-20-4607-2020, 2020.

877 Isaacman-VanWertz, G. and Aumont, B.: Impact of organic molecular structure on the estimation of
878 atmospherically relevant physicochemical parameters, Atmos. Chem. Phys., 21(8), 6541-6563,
879 doi:10.5194/acp-21-6541-2021, 2021.

880 Jenkin, M. E., Saunders, S. M., Wagner, V. and Pilling, M. J.: Protocol for the development of the Master
881 Chemical Mechanism, MCM v3 (Part B): tropospheric degradation of aromatic volatile organic
882 compounds, Atmos. Chem. Phys., 3(1), 181–193, doi:10.5194/acp-3-181-2003, 2003.

883 Jenkin, M. E., Young, J. C. and Rickard, A. R.: The MCM v3.3.1 degradation scheme for isoprene, Atmos.
884 Chem. Phys., 15(20), 11433–11459, doi:10.5194/acp-15-11433-2015, 2015.

885 Kang, E., Root, M. J., Toohey, D. W. and Brune, W. H.: Introducing the concept of Potential Aerosol Mass
886 (PAM), Atmos. Chem. Phys., 7(22), 5727–5744, doi:10.5194/acp-7-5727-2007, 2007.

887 Keller-Rudek, H., Moortgat, G. K., Sander, R. and Sörensen, R.: The MPI-Mainz UV/VIS Spectral Atlas of
888 Gaseous Molecules of Atmospheric Interest, [online] Available from: www.uv-vis-spectral-atlas-
889 mainz.org (Accessed 26 March 2019), 2020.

890 Kovacs, T. A. and Brune, W. H.: Total OH loss rate measurement, J. Atmos. Chem., 39(2), 105–122,
891 doi:10.1023/A:1010614113786, 2001.

892 Krechmer, J. E., Pagonis, D., Ziemann, P. J. and Jimenez, J. L.: Quantification of Gas-Wall Partitioning in
893 Teflon Environmental Chambers Using Rapid Bursts of Low-Volatility Oxidized Species Generated in
894 Situ, Environ. Sci. Technol., 50(11), 5757–5765, doi:10.1021/acs.est.6b00606, 2016.

895 Krechmer, J. E., Day, D. A., Ziemann, P. J. and Jimenez, J. L.: Direct Measurements of Gas/Particle
896 Partitioning and Mass Accommodation Coefficients in Environmental Chambers, Environ. Sci. Technol.,
897 51(20), 11867–11875, doi:10.1021/acs.est.7b02144, 2017.

898 Kwok, E. and Atkinson, R.: Estimation of hydroxyl radical reaction rate constants for gas-phase organic
899 compounds using a structure-reactivity relationship: An update, Atmos. Environ., 29(14), 1685–1695,
900 doi:10.1016/1352-2310(95)00069-B, 1995.

901 Lee-Taylor, J., Hodzic, A., Madronich, S., Aumont, B., Camredon, M., and Valorso, R.: Multiday
902 production of condensing organic aerosol mass in urban and forest outflow, Atmos. Chem. Phys., 15(2),
903 595–615, doi:10.5194/acp-15-595-2015, 2015.

904 Levy II, H.: Normal atmosphere: large radical and formaldehyde concentrations predicted., Science,
905 173(3992), 141–143, doi:10.1126/science.173.3992.141, 1971.

906 Li, R., Palm, B. B., Ortega, A. M., Hu, W., Peng, Z., Day, D. A., Knote, C., Brune, W. H., de Gouw, J. and
907 Jimenez, J. L.: Modeling the radical chemistry in an Oxidation Flow Reactor (OFR): radical formation and
908 recycling, sensitivities, and OH exposure estimation equation, J. Phys. Chem. A, 119(19), 4418–4432,
909 doi:10.1021/jp509534k, 2015.

910 Liu, X., Day, D. A., Krechmer, J. E., Brown, W., Peng, Z., Ziemann, P. J. and Jimenez, J. L.: Direct

measurements of semi-volatile organic compound dynamics show near-unity mass accommodation coefficients for diverse aerosols, Commun. Chem., 2(1), 98, doi:10.1038/s42004-019-0200-x, 2019.

Lu, K. D., Hofzumahaus, A., Holland, F., Bohn, B., Brauers, T., Fuchs, H., Hu, M., Häseler, R., Kita, K., Kondo, Y., Li, X., Lou, S. R., Oebel, A., Shao, M., Zeng, L. M., Wahner, A., Zhu, T., Zhang, Y. H. and Rohrer, F.: Missing OH source in a suburban environment near Beijing: observed and modelled OH and HO 2 concentrations in summer 2006, Atmos. Chem. Phys., 13(2), 1057–1080, doi:10.5194/acp-13-1057-2013, 2013.

Madronich, S. and Flocke, S.: The Role of Solar Radiation in Atmospheric Chemistry, in Environmental Photochemistry. The Handbook of Environmental Chemistry (Reactions and Processes), vol 2 / 2L, edited by P. Boule, pp. 1–26, Springer, Berlin, Heidelberg., 1999.

Mao, J., Ren, X., Brune, W. H., Olson, J. R., Crawford, J. H., Fried, a., Huey, L. G., Cohen, R. C., Heikes, B., Singh, H. B., Blake, D. R., Sachse, G. W., Diskin, G. S., Hall, S. R. and Shetter, R. E.: Airborne measurement of OH reactivity during INTEX-B, Atmos. Chem. Phys., 9(1), 163–173, doi:10.5194/acp-9-163-2009, 2009.

Matsunaga, A. and Ziemann, P. J.: Gas-Wall Partitioning of Organic Compounds in a Teflon Film Chamber and Potential Effects on Reaction Product and Aerosol Yield Measurements, Aerosol Sci. Technol., 44(10), 881–892, doi:10.1080/02786826.2010.501044, 2010.

Mouchel-Vallon, C., Lee-Taylor, J., Hodzic, A., Artaxo, P., Aumont, B., Camredon, M., Gurarie, D., Jimenez, J.-L., Lenschow, D. H., Martin, S. T., Nascimento, J., Orlando, J. J., Palm, B. B., Shilling, J. E., Shrivastava, M. and Madronich, S.: Exploration of oxidative chemistry and secondary organic aerosol formation in the Amazon during the wet season: explicit modeling of the Manaus urban plume with GECKO-A, Atmos. Chem. Phys., 20(10), 5995–6014, doi:10.5194/acp-20-5995-2020, 2020.

Nakashima, Y., Tsurumaru, H., Imamura, T., Bejan, I., Wenger, J. C. and Kajii, Y.: Total OH reactivity measurements in laboratory studies of the photooxidation of isoprene, Atmos. Environ., 62, 243–247, doi:10.1016/j.atmosenv.2012.08.033, 2012.

Nannoolal, Y., Rarey, J. and Ramjugernath, D.: Estimation of pure component properties part 3. Estimation of the vapor pressure of non-electrolyte organic compounds via group contribution and group interactions, Fluid Phase Equilib., 269, 117–133, doi:10.1016/j.fluid.2008.04.020, 2008.

Nehr, S., Bohn, B., Fuchs, H., Häseler, R., Hofzumahaus, A., Li, X., Rohrer, F., Tillmann, R. and Wahner, A.: Atmospheric photochemistry of aromatic hydrocarbons: OH budgets during SAPHIR chamber experiments, Atmos. Chem. Phys., 14(13), 6941–6952, doi:10.5194/acp-14-6941-2014, 2014.

Nel, A.: Air Pollution-Related Illness: Effects of Particles, Science (80-.)., 308(5723), 804–806, doi:10.1126/science.1108752, 2005.

Nguyen, T. B., Crounse, J. D., Schwantes, R. H., Teng, A. P., Bates, K. H., Zhang, X., St. Clair, J. M., Brune, W. H., Tyndall, G. S., Keutsch, F. N., Seinfeld, J. H., and Wennberg, P. O.: Overview of the Focused Isoprene eXperiment at the California Institute of Technology (FIXCIT): mechanistic chamber studies on the oxidation of biogenic compounds, Atmos. Chem. Phys., 14, 13531–13549, 2014.

Nölscher, A. C., Butler, T., Auld, J., Veres, P., Muñoz, A., Taraborrelli, D., Vereecken, L., Lelieveld, J. and Williams, J.: Using total OH reactivity to assess isoprene photooxidation via measurement and model, Atmos. Environ., 89, 453–463, doi:10.1016/j.atmosenv.2014.02.024, 2014.

Nölscher, A. C., Yañez-Serrano, A. M., Wolff, S., de Araujo, A. C., Lavrič, J. V., Kesselmeier, J. and Williams, J.: Unexpected seasonality in quantity and composition of Amazon rainforest air reactivity, Nat. Commun., 7, 10383, doi:10.1038/ncomms10383, 2016.

Novelli, A., Kaminski, M., Rolletter, M., Acir, I. H., Bohn, B., Dorn, H. P., Li, X., Lutz, A., Nehr, S., Rohrer, F., Tillmann, R., Wegener, R., Holland, F., Hofzumahaus, A., Kiendler-Scharr, A., Wahner, A., and Fuchs, H.: Evaluation of OH and HO2 concentrations and their budgets during photooxidation of 2-methyl-3-butene-2-ol (MBO) in the atmospheric simulation chamber SAPHIR, Atmos. Chem. Phys., 18, 11409-11422, doi:10.5194/acp-18-11409-2018, 2018.

Orlando, J. J. and Tyndall, G. S.: Laboratory studies of organic peroxy radical chemistry: an overview with emphasis on recent issues of atmospheric significance, Chem. Soc. Rev., 41(19), 6294–6317, doi:10.1039/c2cs35166h, 2012.

Pankow, J. F. and Asher, W. E.: SIMPOL.1: A simple group contribution method for predicting vapor pressures and enthalpies of vaporization of multifunctional organic compounds, Atmos. Chem. Phys., 8(10), 2773–2796, doi:10.5194/acp-8-2773-2008, 2008.

Peng, Z. and Jimenez, J. L.: Modeling of the chemistry in oxidation flow reactors with high initial NO, Atmos. Chem. Phys., 17(19), 11991–12010, doi:10.5194/acp-17-11991-2017, 2017.

Peng, Z. and Jimenez, J. L.: KinSim: A Research-Grade, User-Friendly, Visual Kinetics Simulator for Chemical-Kinetics and Environmental-Chemistry Teaching, J. Chem. Educ., 96(4), 806–811, doi:10.1021/acs.jchemed.9b00033, 2019.

Peng, Z. and Jimenez, J. L.: Radical chemistry in oxidation flow reactors for atmospheric chemistry research, Chem. Soc. Rev., doi:10.1039/C9CS00766K, 2020.

Peng, Z., Day, D. A., Stark, H., Li, R., Lee-Taylor, J., Palm, B. B., Brune, W. H. and Jimenez, J. L.: HOx radical chemistry in oxidation flow reactors with low-pressure mercury lamps systematically examined by modeling, Atmos. Meas. Tech., 8(11), 4863–4890, doi:10.5194/amt-8-4863-2015, 2015.

Peng, Z., Day, D. A., Ortega, A. M., Palm, B. B., Hu, W., Stark, H., Li, R., Tsigaridis, K., Brune, W. H. and Jimenez, J. L.: Non-OH chemistry in oxidation flow reactors for the study of atmospheric chemistry systematically examined by modeling, Atmos. Chem. Phys., 16(7), 4283–4305, doi:10.5194/acp-16-4283-2016, 2016.

Peng, Z., Palm, B. B., Day, D. A., Talukdar, R. K., Hu, W., Lambe, A. T., Brune, W. H. and Jimenez, J. L.: Model Evaluation of New Techniques for Maintaining High-NO Conditions in Oxidation Flow Reactors for the Study of OH-Initiated Atmospheric Chemistry, ACS Earth Sp. Chem., 2(2), 72–86, doi:10.1021/acsearthspacechem.7b00070, 2018.

Peng, Z., Lee-Taylor, J., Orlando, J. J., Tyndall, G. S. and Jimenez, J. L.: Organic peroxy radical chemistry in oxidation flow reactors and environmental chambers and their atmospheric relevance, Atmos. Chem. Phys., 19(2), 813–834, doi:10.5194/acp-19-813-2019, 2019.

Rohrer, F., Bohn, B., Brauers, T., Brüning, D., Johnen, F.-J., Wahner, A., and Kleffmann, J.: Characterisation of the photolytic HONO-source in the atmosphere simulation chamber SAPHIR, https://doi.org/10.5194/acp-5-2189-2005, 2005.

Sato, K., Nakashima, Y., Morino, Y., Imamura, T., Kurokawa, J. and Kajii, Y.: Total OH reactivity measurements for the OH-initiated oxidation of aromatic hydrocarbons in the presence of NO x, Atmos. Environ., 171, 272–278, doi:10.1016/j.atmosenv.2017.10.036, 2017.

Schwantes, R. H., Schilling, K. A., McVay, R. C., Lignell, H., Coggon, M. M., Zhang, X., Wennberg, P. O. and Seinfeld, J. H.: Formation of highly oxygenated low-volatility products from cresol oxidation, Atmos. Chem. Phys., 17(5), 3453–3474, doi:10.5194/acp-17-3453-2017, 2017.

Siese, M., Becker, K. H., Brockmann, K. J., Geiger, H., Hofzumahaus, A., Holland, F., Mihelcic, D., and Wirtz, K.: Direct measurement of OH radicals from ozonolysis of selected alkenes: a EUPHORE simulation chamber study, Environ. Sci. Technol., 35, 4660–4667, 2001.

Stocker, T. F., Qin, D., Plattner, G.-K., Tignor, M., Allen, S. K., Boschung, J., Nauels, A., Xia, Y., Bex, V. and Midgley, P. M.: Climate Change 2013 - The Physical Science Basis, edited by Intergovernmental Panel on Climate Change, Cambridge University Press, Cambridge., 2014.

Stone, D., Whalley, L. K. and Heard, D. E.: Tropospheric OH and HO2 radicals: field measurements and model comparisons, Chem. Soc. Rev., 41(19), 6348, doi:10.1039/c2cs35140d, 2012.

Turro, N. J., Ramamurthy, V. and Scaiano, J. C.: Principles of Molecular Photochemistry: An Introduction, University Science Books, Sausalito, CA, USA. [online] Available from: http://www.uscibooks.com/turro2.htm, 2009.

US EPA: Estimation Programs Interface SuiteTM, 2012.

Valorso, R., Aumont, B., Camredon, M., Raventos-Duran, T., Mouchel-Vallon, C., Ng, N. L., Seinfeld, J. H., Lee-Taylor, J. and Madronich, S.: Explicit modelling of SOA formation from α-pinene photooxidation: sensitivity to vapour pressure estimation, Atmos. Chem. Phys., 11(14), 6895–6910, doi:10.5194/acp-11-6895-2011, 2011.

Verwer, J. G.: Gauss–Seidel Iteration for Stiff ODES from Chemical Kinetics, SIAM J. Sci. Comput., 15(5),

1012   1243–1250, doi:10.1137/0915076, 1994.

1013   Verwer, J. G., Blom, J. G., van Loon, M. and Spee, E. J.: A comparison of stiff ODE solvers for atmospheric
1014   chemistry problems, Atmos. Environ., 30(1), 49–58, doi:10.1016/1352-2310(95)00283-5, 1996.

1015   Wennberg, P. O., Bates, K. H., Crounse, J. D., Dodson, L. G., McVay, R. C., Mertens, L. A., Nguyen, T. B.,
1016   Praske, E., Schwantes, R. H., Smarte, M. D., St Clair, J. M., Teng, A. P., Zhang, X. and Seinfeld, J. H.: Gas-
1017   Phase Reactions of Isoprene and Its Major Oxidation Products, Chem. Rev., 118(7), 3337–3390,
1018   doi:10.1021/acs.chemrev.7b00439, 2018.

1019   Whalley, L. K., Stone, D., Bandy, B., Dunmore, R., Hamilton, J. F., Hopkins, J., Lee, J. D., Lewis, A. C. and
1020   Heard, D. E.: Atmospheric OH reactivity in central London: observations, model predictions and
1021   estimates of in situ ozone production, Atmos. Chem. Phys., 16(4), 2109–2122, doi:10.5194/acp-16-
1022   2109-2016, 2016.

1023   Williams, J. and Brune, W.: A roadmap for OH reactivity research, Atmos. Environ., 106, 371–372,
1024   doi:10.1016/j.atmosenv.2015.02.017, 2015.

1025   Wofsy, S. C., Apel, E., Blake, D. R., Brock, C. A., Brune, W. H., Bui, T. P., Daube, B. C., Dibb, J. E., Diskin,
1026   G. S., Elkiins, J. W., Froyd, K., Hall, S. R., Hanisco, T. F., Huey, L. G., Jimenez, J. L., McKain, K., Montzka,
1027   S. A., Ryerson, T. B., Schwarz, J. P., Stephens, B. B., Weinzierl, B. and Wennberg, P.: ATom: Merged
1028   Atmospheric Chemistry, Trace Gases, and Aerosols, Oak Ridge, Tennessee, USA., 2021.

1029   Yang, Y., Shao, M., Wang, X., Nölscher, A. C., Kessel, S., Guenther, A. and Williams, J.: Towards a
1030   quantitative understanding of total OH reactivity: A review, Atmos. Environ., 134(2), 147–161,
1031   doi:10.1016/j.atmosenv.2016.03.010, 2016.

1032   Zannoni, N., Gros, V., Lanza, M., Sarda, R., Bonsang, B., Kalogridis, C., Preunkert, S., Legrand, M.,
1033   Jambert, C., Boissard, C. and Lathiere, J.: OH reactivity and concentrations of biogenic volatile organic
1034   compounds in a Mediterranean forest of downy oak trees, Atmos. Chem. Phys., 16(3), 1619–1636,
1035   doi:10.5194/acp-16-1619-2016, 2016.

1036   Ziemann, P. J. and Atkinson, R.: Kinetics, products, and mechanisms of secondary organic aerosol
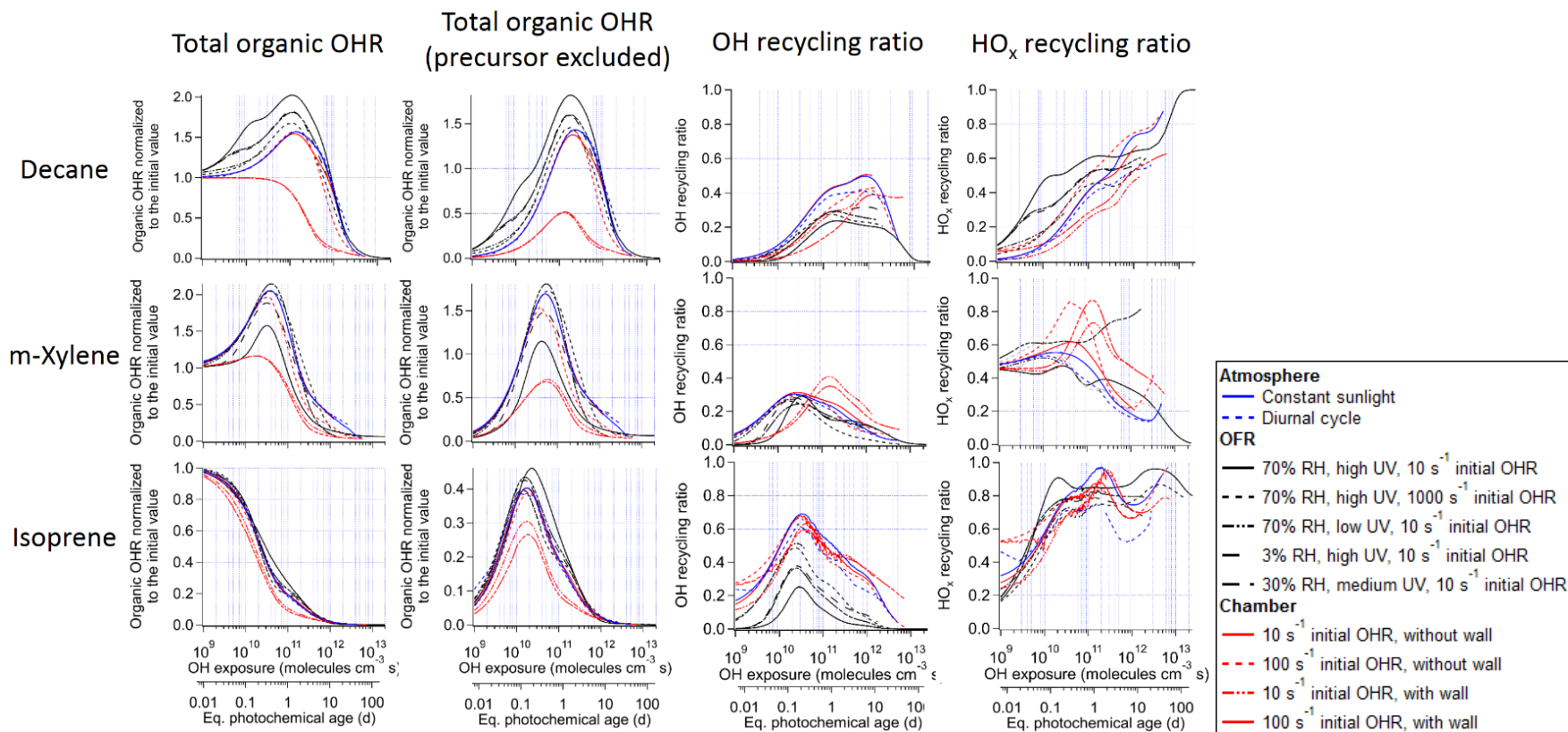1037   formation, Chem. Soc. Rev., 41(19), 6582–6605, doi:10.1039/c2cs35122f, 2012.

Figure 1. Total organic OH reactivity (OHR) with and without the contribution of the precursor, OH recycling ratio (β_1), and HO_x recycling ratio (β_2) as a function of OH exposure (or equivalent photochemical age; second x-axis) in the photooxidations of decane, isoprene, and m-xylene under different conditions in the atmosphere, oxidation flow reactor (OFR), and chamber.
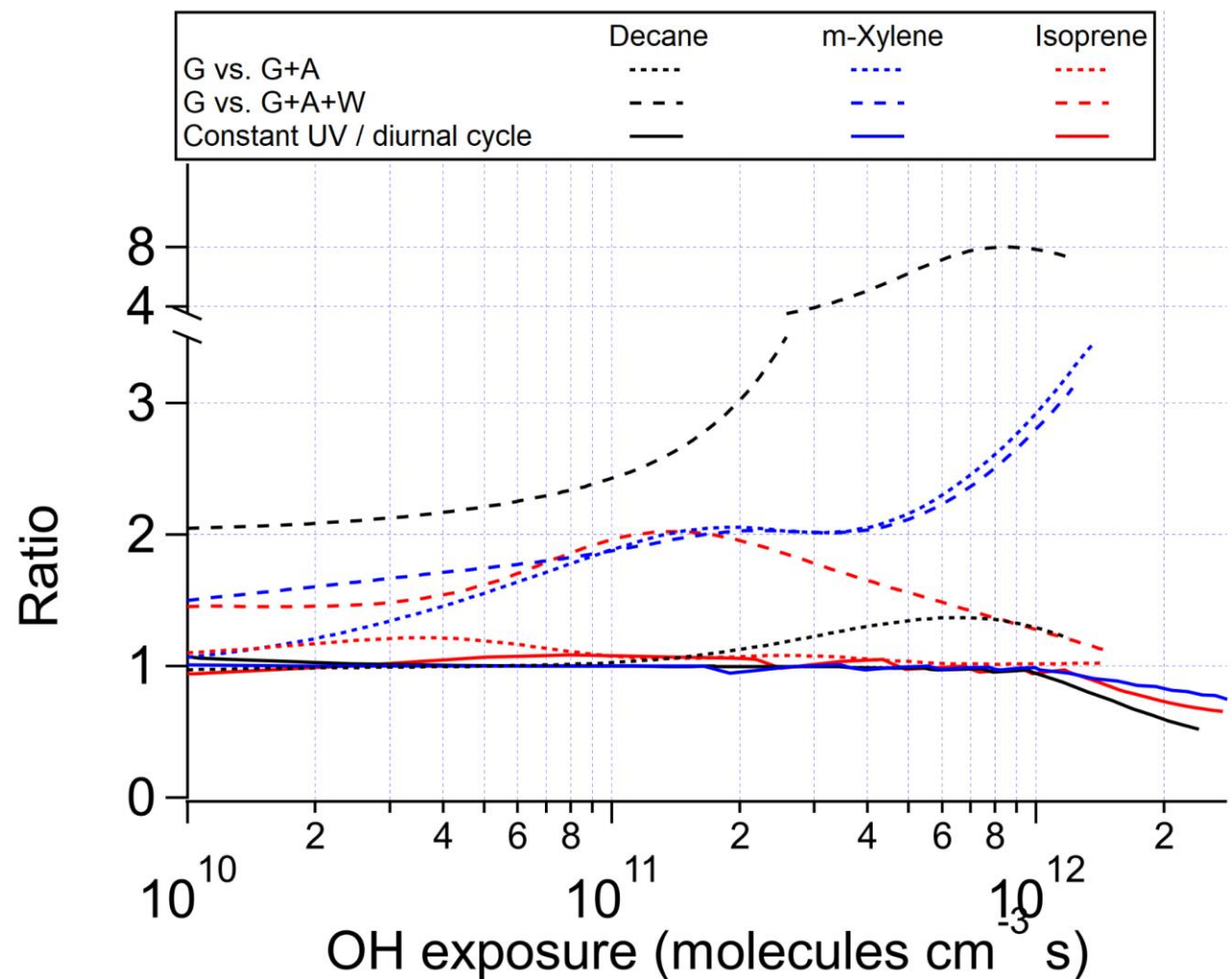
Figure 2. Ratios of OHR of the products present in the gas phase between the chamber cases without gas-particle-wall partitioning and i) with gas-particle (G vs. G+A) or ii) gas-particle-wall partitioning (G vs. G+A+W) at initial OHR of 10 s^{-1}, and between the ambient cases with constant and diurnal sunlight for the photooxidations of decane, m-xylene, and isoprene as a function of OH exposure.
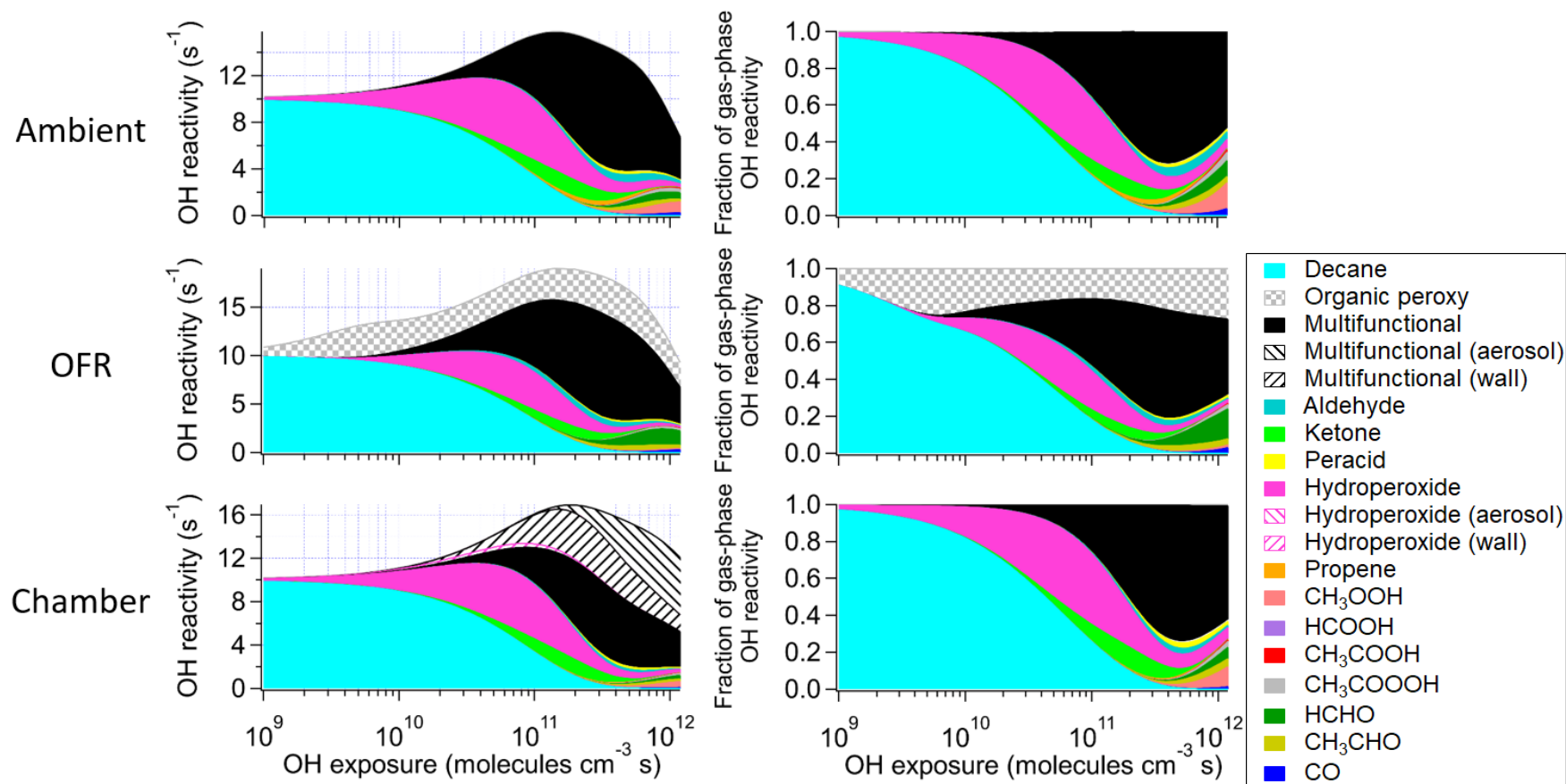
Figure 3. Absolute and fractional contributions to the organic OHR during decane photooxidation of the main species and types of species as a function of OH exposure in the ambient case with constant sunlight; the OFR case with relative humidity of 30%, medium UV lamp setting, and initial OHR of 10 s^{-1}; and the chamber case with initial OHR of 10 s^{-1} and gas-wall partitioning. The types of species shown in this figure exclude the C1 and C2 species listed separately. The OHR of the particle- and wall-phase species are the values as if those species are gas-phase OHR contributors, although they actually do not react with OH in the simulations.
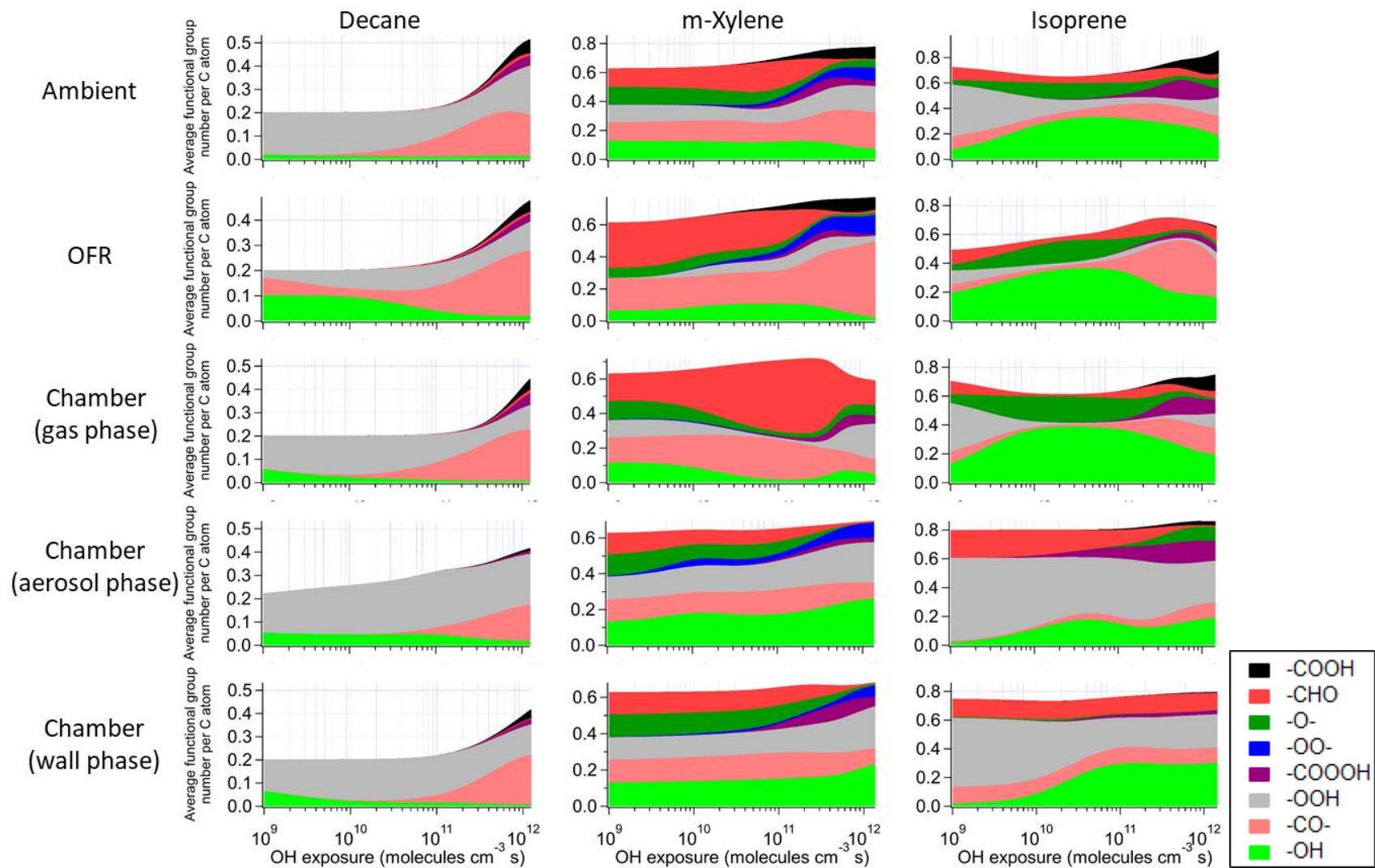
Figure 4. Average number of functional group per C atom as a function of OH exposure in the saturated multifunctional species in the ambient case with constant sunlight, the OFR case with relative humidity of 70%, high UV lamp setting, and initial OHR of 10 s⁻¹, and the gas, aerosol, and wall phases in the chamber case with initial OHR of 10 s-1 and gas-particle-wall partitioning of the photooxidations of decane, m-xylene, and isoprene. Note that the functional group "-O-" represents

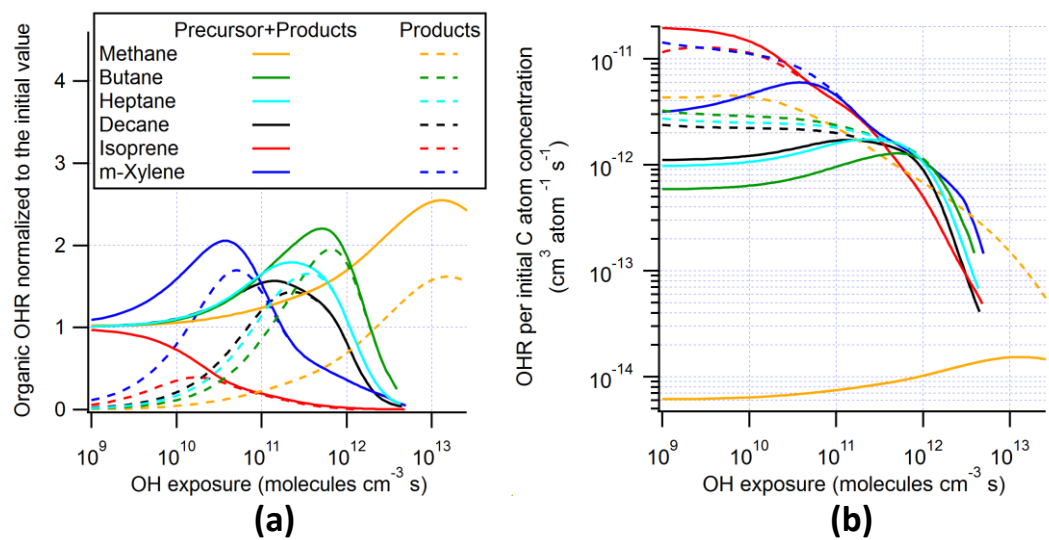ether, ester, and epoxy groups in the GECKO-A model.

Figure 5. (a) OHR and (b) OHR per initial C atom concentration of the organics (including and excluding the precursor) as a function of OH exposure in the ambient cases with constant sunlight of the photooxidation of methane, butane, heptane, decane, isoprene, and m-xylene.
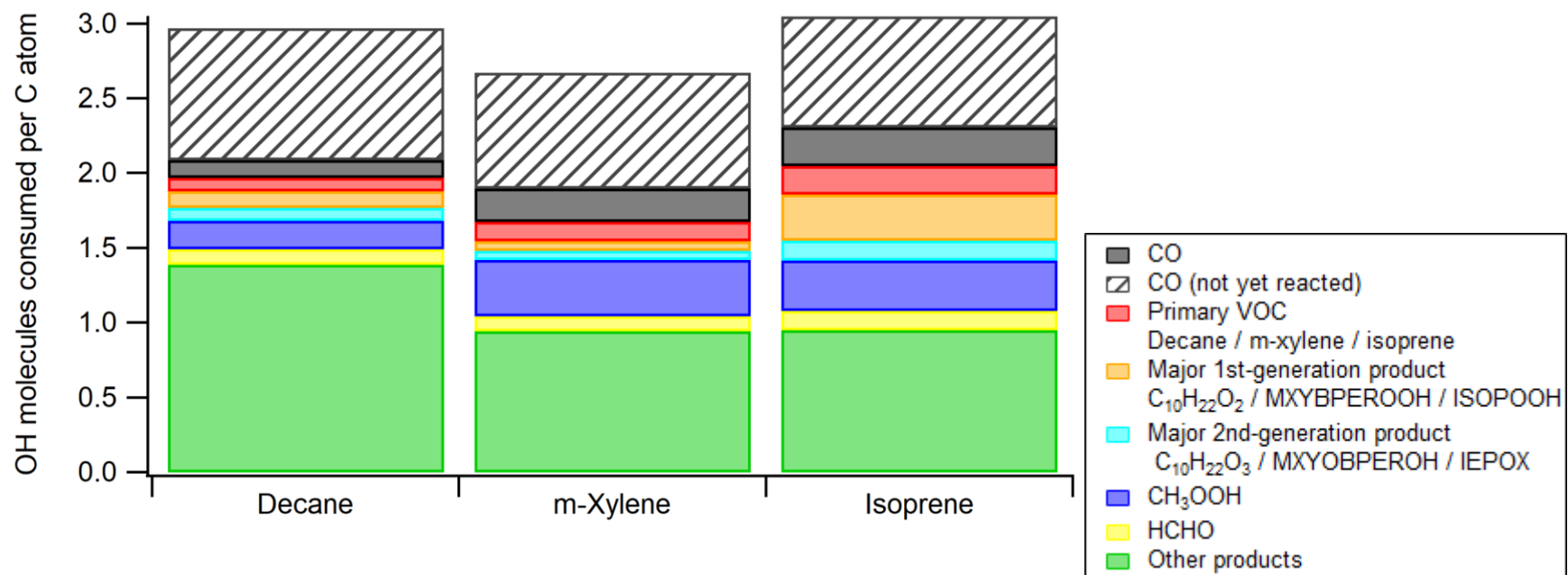
Figure 6. Average numbers of OH molecules consumed per C atom in the ambient cases with constant sunlight during photooxidation of isoprene, decane, and m-xylene. The contribution from CO that is not yet oxidized by OH at the end of simulation is also added to ensure that each CO molecule consumed one OH radical. ISOPOOH, IEPOX, $C_{10}H_{22}O_2$, and $C_{10}H_{22}O_3$ are isoprene hydroxyl hydroperoxides, isoprene epoxydiols, decyl hydroperoxides, and hydroxydecyl hydroperoxides, respectively. See Scheme S1 for the structures of MXYBPEROOH and MXYOBPEROH.

Table 1. Conditions and integration timesteps of the simulations in the present work.

Precursor	Environment	Relative humidity (%)	UV	Initial OH reactivity (s⁻¹)	Integration timestep (s)
Methane	Ambient	30	Constant sunlight[a]	10	KinSim-determined[b]
	Oxidation flow reactor	70	High lamp setting[c]		
Decane	Ambient	30	Constant sunlight[a]	10	Min: 0.1; Max: 120 (1 d), 300 (2–10 d)
			Diurnal sunlight		
	Oxidation flow reactor	70	High lamp setting[c]	10	0.0025
		70	Low lamp setting[e]	10	
		30	Medium lamp setting[f]	10	
		3	High lamp setting[c]	10	
		70	High lamp setting[c]	1000	
	Chamber (gas-phase only)	30	CU Chamber spectrum[g]	10	Min: 0.1; Max: 120 (6 d), 300 (7–30 d if needed)
				100	
	Chamber (gas-particle partitioning)			10	
				100	
	Chamber (gas-particle -wall partitioning)			10	
				100	
m-Xylene	Ambient	30	Constant sunlight[a]	10	Min: 0.1; Max: 120 (1 d), 300 (2–10 d)
			Diurnal sunlight[c]		
	Oxidation flow reactor	70	High lamp setting[c]	10	0.0025
		70	Low lamp setting[e]	10	
		30	Medium lamp setting[f]	10	
		3	High lamp setting[c]	10	
		70	High lamp setting[c]	1000	
	Chamber (gas-phase only)	30	CU Chamber spectrum[g]	10	Min: 0.1; Max: 120 (6 d), 300 (7–30 d if needed)
				100	
	Chamber (gas-particle partitioning)			10	
				100	
	Chamber (gas-particle -wall partitioning)			10	
				100	
Isoprene	Ambient	30	Constant sunlight[a]	10	Min: 0.1; Max: 10 (1 d), 120 (2–10 d)
			Diurnal sunlight[c]		
	Oxidation flow reactor	70	High lamp setting[c]	10	0.001
		70	Low lamp setting[e]	10	
		30	Medium lamp setting[f]	10	
		3	High lamp setting[c]	10	
		70	High lamp setting[c]	1000	
		30	Medium lamp setting[f] + 5x CU Chamber spectrum[g]	10	

		30	Medium lamp setting[f] + 10000x CU Chamber spectrum[g]	10	
	Chamber (gas-phase only)			10	
				100	
	Chamber (gas-particle partitioning)	30	CU Chamber spectrum[g]	10	Min: 0.1; Max: 10 (6 d), 120 (7–30 d if needed)
				100	
	Chamber (gas-particle -wall partitioning)			10	
				100	
Butane	Ambient	30	Constant sunlight[a]	10	Min: 0.1; Max: 120 (1 d), 300 (2–10 d)
Heptane	Ambient	30	Constant sunlight[a]	10	Min: 0.1; Max: 120 (1 d), 300 (2–10 d)

[a] At solar zenith angle of 45°.

[b] Simulation performed in the solver KinSim, which fully controls its integration timestep selection.

[c] Diurnal variation between solar zenith angles of 0 and 90°.

[d] UV at 185 nm = 1×10^{14} photons cm^{-2} s^{-1}; UV at 254 nm = 8.5×10^{15} photons cm^{-2} s^{-1}.

[e] UV at 185 nm = 1×10^{11} photons cm^{-2} s^{-1}; UV at 254 nm = 4.2×10^{13} photons cm^{-2} s^{-1}.

[f] UV at 185 nm = 1×10^{13} photons cm^{-2} s^{-1}; UV at 254 nm = 1.4×10^{15} photons cm^{-2} s^{-1}.

[g] UV source spectrum of the University of Colorado Environmental Chamber Facility (Krechmer et al., 2017).